Ray Tracing of Microwaves in Fusion Plasmas

By
Victor Lorentzen (s183753)

Supervisors:
Stefan Kragh Nielsen & Mads Givskov Senstius
Section for Plasma Physics and Fusion Energy
Department of Physics

Acknowledgements

Abstract

Increasing energy consumption generates necessity for effective, reliable energy sources. Fusion energy focusing on the fusion of hydrogen isotopes is a promising future energy source and is possible in burning plasmas at high temperatures of 100s of millions of Kelvins. Heating of plasmas are done for example by using cyclotron resonance heating done by injection of polarised electromagnetic waves, ordinary and extraordinary modes, with frequencies around the harmonics of the cyclotron resonance frequency. Diagnostics of plasmas are also done using wave injection of high power microwaves, while other methods exist. Observations of anomalous scattering during injection of microwaves suggest nonlinearities resulting from wave-plasma interactions in non-monotonic density structures called islands. Since the electromagnetic waves cannot propagate through plasmas of very high densities it is important to have tools to determine the beam trajectories. Althgouh it is possible to trace the propagating waves using full wave simulations, which are done by solving Maxwell's equations for tokamak-geometry exactly, the full wave simulations are numerically expensive. A good substitute is ray tracing made by assumptions when considering wave propagations in plasma. Plasmas are often considered dielectric materials, thus geometrical optics presents itself as a ray tracing opportunity.
In this thesis a ray tracer has been made in order to trace the beams injected into a fusion plasma artificially designed to mimic tokamaks. The ray tracer utilizes the Appleton-Hartree dispersion relation for ordinary and extraordinary waves, O- and X-mode waves, and a kinetic dispersion relation for X-mode- and electrostatic waves called Electron Bernstein Waves or EBWs. Propagations of O-mode-, X-mode- and EBWs have been simulated through synthetic, tokamak-like density structures for verification and visualization, including density structures with an island. Convergence checks of the ray tracer have been made in comparison with theoretical values to find appropriate numerical step sizes needed.
The simulated wave trajectories using the ray tracer made for this project are found to be accurate given small enough numerical steps depending on the wave-mode. The O-mode-, X-mode- and EBWs propagate as expected and are stopped by the relevant cutoffs. Investigations of slow X-mode and EBWs using the kinetic dispersion relation with the ray tracer show a possible entrapment of the waves. Furthermore, the simulations using the ray tracer show that slow X-mode waves and EBWs can be trapped in islands and can lead to cavities and non-linear effects.

Contents

1 Introduction

1.1 Fusion Energy

Energy consumption rises every year, and with the increasing interest in and need for renewable energy sources, fusion energy poses a great solution to this problem as a source of nearly inexhaustible energy source [5]. Nuclei are held together by the strong nuclear force with a binding energy. For nuclei with masses below the mass of an iron nucleus, the fusion or combination of two nuclei releases energy as the sum of the binding energies of the separate nuclei is greater than the binding energy of the fused nuclei. Fusion energy revolves around the fusion of hydrogen isotopes deuterium and tritium, which can be found in seawater and produced by irradiating Lithium respectively, where the released energies of hydrogen and helium reactions are [5][8][12]

$$D + D \rightarrow {}^3He + n + 3.27\,MeV, \tag{1.1}$$

$$D + {}^3He \rightarrow {}^4He + p + 18.3\,MeV, \tag{1.2}$$

$$D + T \rightarrow {}^4He + n + 17.6\,MeV. \tag{1.3}$$

Since tritium is highly unstable, irradiation of lithium must be done to obtain it:

$$^6Li + n \rightarrow {}^4He + T + 4.8\,MeV, \tag{1.4}$$

$$^7Li + n \rightarrow {}^4He + T + n - 2.5\,MeV. \tag{1.5}$$

Just as the sun fuses hydrogen to release energy, researchers and investors also seek to utilize this fusion process to generate energy. Currently, a testing facility fusion reactor ITER is under construction in France, and is expected to return energy output tenfold the heating power input [10]. In order to reach this potential, a fusion reactor must reach ignition. Ignition occurs when the output energy is greater than the input energy. This is known as the Lawson criterion[3][4][12], often described as the triple product $nT\tau$, where n is the particle density, T is the temperature and τ is the confinement time. Using a Deuterium-Tritium plasma, ignition requires a triple product of $nT\tau = 3\,10^{21}\,keV\,s\,m^{-3}$. This requires temperatures of $T = [10, 20]\,keV$ or $T = 116\,10^6 - 232\,10^6\,K$ [12].

A popular method of containing burning plasma at high temperature is the tokamak. An example can be seen in Fig. 1 from [10]. Here a toroidal magnetic field is present due to the electric coil system surrounding the torus shaped container, resulting in both poloidal and toroidal electric and magnetic fields. Note that the magnetic field on the outer rim of the plasma (purple in Fig. 1) are not only in the toroidal direction, but also have a poloidal component. The magnetic field is designed to contain charged particles, and in order to do so, the resulting magnetic field often surrounds the torus in a helix shaped field. The container is not entirely cylindrical in the cross section, but more of a "D" shape. The complete structure of a tokamak is quite complex and can vary depending on the size and the intended size, temperatures and densities. At these high temperatures, electrons are effectively separated from the nuclei, resulting in a cloud of charged particles, namely ions and electrons, and neutrons. The charged particles are contained due to the magnetic field, but the neutrons are not. According to Iter.org [10], 80 % of the generated energy is carried away by the neutrons, which then collide with the tokamak walls as they are not contained by the magnetic field. The kinetic energy carried is then converted to electrical energy for example by generating steam that powers turbines.

1.2 Microwave Technology, Heating Schemes and Diagnostics

There are three major heating schemes for heating a plasma to the intended high temperatures: 1) Ohmic heating relying on the effect of the induced electric current in the plasma, $P = I^2R$. The resistance is dependent on electron-ion collisions which decreases as temperature rises, so as the
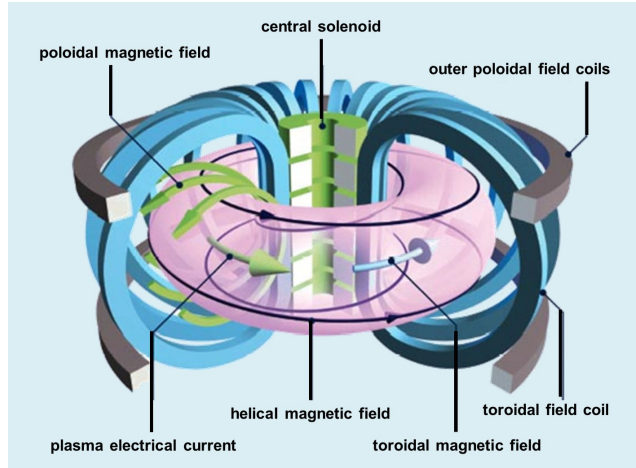
Figure 1: The illustration depicts a torus shaped tokamak, which is currently the strongest way to confine plasma with a toroidal magnetic field. Surrounding the Torus is a coil structure built to induce a magnetic field through the torus with a magnetic field strength at the orders of magnitude $0.1 - 10\,\text{T}$ and a magnetic field around it. The goal is to contain charged particles within the burning plasma inside the tokamak. The image is from [10].

temperature of the plasma rises towards the intended levels, Ohmic heating becomes gradually less effective. Ohmic heating is thus mainly useful in the ignition phase of plasma heating. 2) Particle heating by a neutral beam injection (NBI) of for example deuterium at high energies ($50 - 500\,\text{keV}$), which are then ionized, slowed and thermalized. In order to reach $1\,\text{MW}$ of heating, 10^{19} particles with an energy of $100\,\text{keV}$ must be injected pr. second [8] (the same order of magnitude as the ion and electron densities), which can result in overdense plasmas where injection beams cannot propagate. 3) Wave heating at the cyclotron resonance frequencies: Electron Cyclotron Resonance Heating (ECRH) for electrons, and correspondingly Ion Cyclotron Resonance Heating (ICRH) for ions. ECRH and ICRH are only possible with waves at frequencies close to the resonances, thus wave heating allows for precision in heating either ions or electrons, and technology has been developed to provide heating powers of tens of MW [5][8]. The frequency range for ECRH is around $50 - 200\,\text{GHz}$, depending on the strength of the magnetic field, thus in the microwave frequency regime.

Diagnostics involves interaction with the plasma and an analysis of the results. Diagnostics are done by particle or wave interaction with the plasma, either actively or inactively. Important characteristics of good diagnostics devices includes having no large disturbance on the plasma and the ability to experimentally determine the important parameters of a plasma, such as the particle densities, temperatures, magnetic field strengths etc. Here, microwave diagnostics of frequency $50 - 200\,\text{GHz}$ are extremely useful, as they probe the material with no material contact [5][8]. Diagnostic devices using microwaves to perform probing send and receive waves to characterize the plasma, thus rendering the devices vulnerable to rogue waves and anomalous scattering. Measurements of unexpected scattering has lead to an added attention to non-linear effects previously not thought relevant for the used reactor parameters. These non-linear effects can be destructive for diagnostics equipment, but also have the potential for heating [8]. Microwave devices are readily available as microwave technology is often used in the food industry and in semiconductor production, which gives ease of access to some of the required technology to perform ECRH and ICRH. Microwaves are currently being used by the Plasma Physics and Fusion Energy group (PPFE) at DTU, department of Physics in NORTH, the groups Tokamak designed for experimentation.

1.3 Ray Tracing and Project Objective

Ray tracing provides a numerical solver for these complex situations. Already in the entertainment and 3D design industries, ray tracing plays a major role. Ray tracing indicates the tracing of a linear, zero-width optical ray [9] through material. In plasma physics, waves are used for both heating schemes and diagnostics, thus the trajectory of said waves is important. Ray tracing makes it possible to simulate wave propagation through fusion plasma [3][12] and know what results to expect from experimentation on a real tokamak. Opposed to full wave simulation, which is to directly solve Maxwell's equations, ray tracing presents a cost efficient numerical solver for beam trajectories.

In this project, a ray tracer is written to calculate beam trajectories through an artificial plasma. In order to do so, the underlying theory of plasma waves, especially the polarised electromagnetic ordinary and extraordinary (O-mode and X-mode) waves that appear by assuming zero temperature and the slow X-mode and electrostatic electron Bernstein waves (EBWs) that appear from a kinetic/warm plasma approach of finite temperatures, must be presented: First going through the fundamental dynamics of charged particles in a plasma, then going through the cold plasma approximation and the kinetic plasma approach. Ray tracing theory and three wave interactions are also presented shortly. After this, the numerical methods and parameter choices for simulations are presented, followed by results of multiple beam tracings through an artificial plasma using the ray tracer. Here verification of the ray tracer is done, while showcasing some possible trajectories in tokamaks with similar geometry, and results of specific cases such as X-mode and EBW trapping simulations are presented.

2 Plasma Theory

2.1 Fundamental Dynamics of Single Charged Particles

A plasma can be described as a quasi-neutral ionized gas, which is dominated by long distance interactions. It can also be viewed as a cloud of ionized particles, where the ions and electrons are separate. Plasmas exist in many places: In stars, interstellar space, fabrication methods and fusion energy to name a few. A plasma is described by the main parameters: the number density n_σ of charged particles with, the temperature T_σ often measured in electron volts and the magnetic field B in Teslas. σ is used as subscript to denote the species of particles; ions or electrons. Since the particles in the plasma are charged, the fundamental equations of plasma physics are the Maxwell equations[3][6],

$$\vec{\nabla} \cdot \vec{E} = \frac{\rho}{\epsilon_0}, \tag{2.1}$$

$$\vec{\nabla} \cdot \vec{B} = 0, \tag{2.2}$$

$$\vec{\nabla} \times \vec{E} = -\frac{\partial \vec{B}}{\partial t}, \tag{2.3}$$

$$\vec{\nabla} \times \vec{B} = \epsilon_0 \mu_0 \frac{\partial \vec{E}}{\partial t} + \mu_0 \vec{J}, \tag{2.4}$$

where $\vec{B}$ and $\vec{E}$ are the magnetic- and electric- fields, ρ is the charge density, $\epsilon_0 \approx 8.85\,10^{-12}\,\mathrm{F\,m^{-1}}$ is the vacuum permitivity, $\mu_0 \approx 1.25\,10^{-6}\,\mathrm{N/A^2}$ the vacuum permeability and $\vec{J}$ the current density. The Lorenz force describes the force acting on a single charged particle due to the surrounding electric- and magnetic fields,

$$\vec{F} = q\left(\vec{E} + \vec{v} \times \vec{B}\right), \tag{2.5}$$

where q and $\vec{v}$ are the charge and velocity of the particle, and $\vec{F}$ is the resulting force. Together, Maxwell's equations and the Lorentz' force lay the foundation for motion of charged particles, i.e. the dynamics of plasmas. The electrostatic electric field resulting from a charged particle can be written in terms of the potential $V(R)$ as a function of the radius R, $\vec{E}(R) = -\vec{\nabla}V(R)$, where $\vec{\nabla}$ denotes the gradient with respect to the spatial coordinates and $V(R)$ is given by the Yukawa potential,

$$V(R) = \frac{q}{4\pi\epsilon_0 R} \exp{-\frac{R}{\lambda_{D_\sigma}}}, \tag{2.6}$$

where λ_{D_σ} corresponds to the Debye length,

$$\lambda_{D_\sigma}^2 = \frac{\epsilon_0 T_\sigma}{n_\sigma q_\sigma^2}, \tag{2.7}$$

which is the shielding radius of the species σ, either ions or electrons. At $R >> \lambda_D$ the potential goes to 0, while at $R < \lambda_D$ the potential is a finite value for $R > 0$, thus showing that the plasma is neutral at distances much larger than the Debye length λ_D [3]. This means that in order to interact with a plasma using electromagnetism, the distance to the particle we wish to interact with has to be low enough compared to the respective temperature and density of that species of particle. For us, that means in order to enable fusion reactions in a space much smaller than the sun, the temperatures must be far greater than the sun's, which is $5788\,\mathrm{K}$. Considering only the velocity component perpendicular to the magnetic field, and remembering that the magnetic and electric fields are perpendicular, the Lorentz force becomes

$$\vec{F} = q v_\perp B. \tag{2.8}$$

Noting that this motion is always circular, the resulting force involving perpendicular velocity is the centripetal force yielding

$$\frac{m v_\perp}{r} = q v_\perp B \iff \frac{v_\perp}{r} = \omega_c = \frac{qB}{m}, \tag{2.9}$$

where ω_c is the cyclotron frequency of the particle. Depending on the species of particle, this frequency is defined as the electron cyclotron resonance (ECR) or the ion cyclotron resonance (ICR). Noting that the mass of an electron compared to the mass of a proton is about $m_e \approx \frac{1}{2000}m_p$. Considering the hydrogen isotope protium, where the nucleus consists of a single proton and no neutrons, the mass of an electron compared to the ion is exactly this fraction. Adding neutrons, as in the case of Deuterium (1 neutron) and Tritium (2 neutrons), the ion mass becomes even greater compared to the electron mass, as neutrons have about the same mass as protons. Since frequencies are positive, the absolute value of the charge is used, and using species notation, the ECR and ICR can be written as $\omega_{c\sigma} = \frac{|q_\sigma|B}{m_\sigma}$, where again σ denotes the species electrons or ions.

In single particle notation the equation of motion using Newton's 2nd law of motion $F = m\,d\vec{v}/dt$ with the Lorentz force becomes

$$m_\sigma \frac{\mathrm{d}}{\mathrm{d}t}\vec{v}_\sigma = q_\sigma \left(\vec{E} + \vec{v}_\sigma \times \vec{B} \right) \tag{2.10}$$

for each species σ. The magnetic field $\vec{B}$ is often defined as only having a component in the z-direction, $\vec{B} = B_0 \hat{z}$. Also defining the electric field to only have a component in the y-direction, $\vec{E} = B_0 \hat{y}$, and then averaging the velocities and assuming the existence of a drift velocity and slow changes in the fields in both space and time, the left hand side of (2.10) becomes 0, and we are left with

$$\vec{0} = \vec{E} + \langle \vec{v}_\sigma \rangle \times \vec{B}, \tag{2.11}$$

with $\langle \vec{v} \rangle$ denoting the average velocity. Ignoring the species for now, the solution to this equation is

$$\langle \vec{v} \rangle = \frac{\vec{E} \times \vec{B}}{B^2}, \tag{2.12}$$

or more generally by substituting $\vec{E} = \frac{\vec{F}}{q}$,

$$\vec{v}_{drift} = \frac{\vec{F} \times \vec{B}}{qB^2}, \tag{2.13}$$

which for any force acting on the particle generates a drifting velocity. This could be an $\vec{E} \times \vec{B}$ drift as shown above. The motion of an ion due to an $\vec{E} \times \vec{B}$ drift can be seen in Fig. 2, where the blue circulating motion displays the cyclotron frequency, and the red line displays the drifting motion of the gyro center of a charged particle. Here as in the derivation, the magnetic field is in the z-direction coming out of the paper while the electric field is in the y-direction. The resulting drift is thus in the $\vec{E} \times \vec{B}$ direction, and the circulation direction is found from (2.9) (or by the left hand rule for ions - with thumb raised in the direction of motion, circulation follows the direction of the remaining fingers. Right hand rule for electrons). The magnetic field in a tokamak must be designed in order to contain the drifting electrons and ions.

2.2 Two-Fluid Approach

Calculations of single particles for large densities required for fusion plasma are costly and would take an unimaginable amount of time to complete. Instead, a two-fluid approach is used. Still based on Maxwell's equations and the Lorentz force, the equations are now looked at in fluids of particles, specifically defining the two plasma fluids; a fluid of electrons and a fluid of ions. Here, the overall charge of the plasma is $q_{Tot} = \sum_\sigma q_\sigma$, which for plasmas of approximately the same electron as ion densities, $n_e \approx n_i$ is $q_{Tot} \approx 0$, thus a plasma as a whole is generally neutral. The mass density is similarly $\rho_{m_{Tot}} = \sum_\sigma m_\sigma n_\sigma$, the charge density $\rho_{q_{Tot}} = \sum_\sigma q_\sigma n_\sigma$ and the current density $\vec{J} = \sum_\sigma q_\sigma n_\sigma \langle \vec{v}_\sigma \rangle$. By Taylor expansion of the electric and magnetic fields and all parameters mentioned here, mainly looking at the 0-th and 1-st order perturbations, i.e. $\vec{E} \approx \vec{E_0} + \vec{E_1}$ and $\vec{B} \approx \vec{B_0} + \vec{B_1}$ for the fields, the consequences of small amplitude field perturbations can be evaluated.
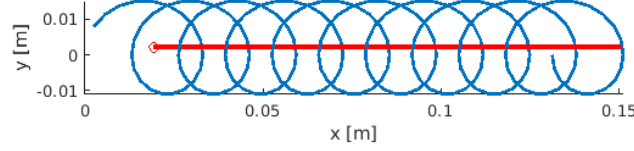
Figure 2: Drift due to external force. The red line is the gyro center motion and the blue curvature is the gyration of the charged particle in an $\vec{E} \times \vec{B}$ - drift. For example in this case, if the force applied to the particle stems from an electric field, then the electric field is going in the y-direction, and the magnetic field goes in the z-direction. This particle is an ion, evident from the direction of circulation.

The 0-th order perturbation is considered generally constant, while the first order perturbation creates responses throughout the plasma. The electric field 1-st order perturbation is assumed to be a plane wave [3][4][12],

$$\vec{E_1}(\vec{r}, t) \sim \exp(i\vec{k} \cdot \vec{r} - i\omega t), \tag{2.14}$$

where $\vec{k}$ is the wave vector with a corresponding wavenumber $k = \sqrt{k_x^2 + k_y^2 + k_z^2}$, $\vec{r}$ is the position vector with components $\vec{r} = (x, y, z)$, ω is the frequency and t the time. In wave theory, $\vec{k}$ is described as a propagation constant responsible for the propagation of the wave with respect to space, and ω the frequency responsible for propagation with respect to time. This linear analysis of a plasma leads to linear waves that are able to propagate through a plasma. Converting the equation of motion (2.10) to fluid notation the particle densities are added such that it becomes

$$m_\sigma n_e \left[\frac{\partial \vec{v_\sigma}}{\partial t} + (\vec{v_\sigma} \cdot \vec{\nabla})\vec{v_\sigma} \right] = q_\sigma n_\sigma (\vec{E} + \vec{v_\sigma} \times \vec{B}) - \vec{\nabla} p_\sigma, \tag{2.15}$$

where $\vec{v_\sigma}$ now corresponds to the fluid velocity of the species σ (ions or electrons) and depends on the density of the particular species, and p_σ is the pressure of the species, which from the equation of state is $p_\sigma = C_\sigma n_\sigma^{\gamma_\sigma}$ with C_σ being the heat capacity and γ_σ the adiabatic index of the species. Together with the continuity equation (conservation of particles),

$$\frac{\partial n_\sigma}{\partial t} + \vec{\nabla} \cdot (n_\sigma \vec{v_\sigma}) = 0, \tag{2.16}$$

Maxwell's equation and the Lorentz force, we now have a full set of equations and parameters to solve. There are many conclusions to draw from these equations, so the first step is to simplify the set. Setting the temperatures to 0 and considering electrostatics with no fluctuating magnetic field $(B_1 \to 0)$, resulting in the plasma frequency,

$$\omega_{p\sigma}^2 = \frac{n_e e^2}{\epsilon_0 m_\sigma} \tag{2.17}$$

The plasma frequency thus corresponds to the electrostatic oscillations of each fluid of species. Letting just the temperatures of the species be 0 and thus removing the pressure dependence, which

6

is called the cold plasma approach, allows us to find more complex linear waves that can propagate through a plasma.

2.3   Cold Plasma Approximation

Setting $T_\sigma \to 0$ and letting the magnetic field be different from zero, we now look to describe the dispersion relations for electromagnetic wave modes in the Cold Plasma limit. In this section conclusions are drawn about the properties of plasma at low temperatures and find out how waves will behave in such an environment via dispersion relations. Starting again with Maxwell's equations (Faraday's and Ampere's Laws),

$$\vec{\nabla} \times \vec{E} = -\frac{\partial \vec{B}}{\partial t}, \tag{2.18}$$

$$\vec{\nabla} \times \vec{B} = \epsilon_0 \mu_0 \frac{\partial \vec{E}}{\partial t} + \mu_0 \vec{J}, \tag{2.19}$$

with $\vec{E}(\vec{r}, t)$ and $\vec{B}(\vec{r}, t)$. Taking the curl of (2.18) and the time derivative of (2.19) yields

$$\vec{\nabla} \times \left(\vec{\nabla} \times \vec{E} \right) + \frac{1}{c^2} \frac{\partial^2}{\partial t^2} \vec{E} + \mu_0 \vec{J} = 0. \tag{2.20}$$

The differential equation can be solved as long as the current density $\vec{J}$ is known. Using the same perturbation theory as in section 2.2, the current density can be written as $\vec{J} = \sum_\sigma q_\sigma n_\sigma \langle \vec{v}_\sigma \rangle$. Noting that the current density and the electric field are related through Ohm's law $\vec{J}_1 = \sum_\sigma \sigma_q \vec{E}_1$, where σ_q is the surface charge density and $\vec{J}_1$ the current density response to the electric field 1-st order perturbation. Since the response is linear, it is convenient to use Laplace-transformation. A plasma can be considered a dielectric of a linear medium, where the two-fluid notation of the current density and the electric displacement are estimated using the sum approximation. Furthering the sum approximation to an integral over all space yields (and for the derivation dropping the perturbation notation $\vec{J}_1$ to just $\vec{J}$),

$$\vec{J}(t, \vec{r}) = \int_{-\infty}^{t} \int \overline{\overline{\sigma}}(t, t', \vec{r}, \vec{r}') \cdot \vec{E}(t', \vec{r}') d\vec{r}' dt', \tag{2.21}$$

$$\vec{D}(t, \vec{r}) = \int_{-\infty}^{t} \int \overline{\overline{\epsilon}}(t, t', \vec{r}, \vec{r}') \cdot \vec{E}(t', \vec{r}') d\vec{r}' dt', \tag{2.22}$$

where $\overline{\overline{\sigma}}$ and $\overline{\overline{\epsilon}}$ are the electric conductivity and dielectric tensors respectively. The plasma is considered homogeneous in both space and time, thus the tensors can be written as functions of $t - t'$ and $\vec{r} - \vec{r}'$ [12]:

$$\vec{J}(t, \vec{r}) = \int_{-\infty}^{t} \int \overline{\overline{\sigma}}(t - t', \vec{r} - \vec{r}') \cdot \vec{E}(t', \vec{r}') d\vec{r}' dt' \tag{2.23}$$

$$\vec{D}(t, \vec{r}) = \int_{-\infty}^{t} \int \overline{\overline{\epsilon}}(t - t', \vec{r} - \vec{r}') \cdot \vec{E}(t', \vec{r}') d\vec{r}' dt', \tag{2.24}$$

Using the small amplitude plane wave perturbation for the electric field,

$$\vec{E}(\vec{r}, t) \sim \exp(i\vec{k} \cdot \vec{r} - i\omega t), \tag{2.25}$$

the Fourier-Laplace transform of the electric field can thus be defined as

$$\vec{E}(\omega, \vec{k}) = \int_{0}^{\infty} \int \vec{E}(t, \vec{r}) \exp(-i\vec{k} \cdot \vec{r} + i\omega t) \, d\vec{r} dt \tag{2.26}$$

and the inverse

$$\vec{E}(t, \vec{r}) = \frac{1}{(2\pi)^4} \int \int \vec{E}(\omega, \vec{k}) \exp(i\vec{k} \cdot \vec{r} - i\omega t) \, d\vec{k} d\omega \tag{2.27}$$

Noting the relations between real space and Fourier space the spatial gradients and time derivatives can be swapped,

$$\vec{\nabla} \Rightarrow i\vec{k}, \quad \frac{\partial}{\partial t} \Rightarrow -i\omega, \tag{2.28}$$

such that (2.20) can be rewritten as

$$-\vec{k} \times \left(\vec{k} \times \vec{E} \right) - \frac{\omega^2}{c^2} \vec{E} - i\omega\mu_0 \vec{J} = 0. \tag{2.29}$$

Using Ohm's Law, which is here the convolution in real space in (2.23) and (2.24) and product in Fourier-space,

$$\vec{J}(\omega, \vec{k}) = \bar{\bar{\sigma}}(\omega, \vec{k}) \cdot \vec{E}(\omega, \vec{k}), \tag{2.30}$$

$$\vec{D}(\omega, \vec{k}) = \bar{\bar{\epsilon}}(\omega, \vec{k}) \cdot \vec{E}(\omega, \vec{k}), \tag{2.31}$$

now making (2.20) in terms of $\vec{E}$, $\vec{J}$ and the conductivity tensor

$$\vec{k} \times \left(\vec{k} \times \vec{E} \right) + \frac{\omega^2}{c^2} \left(\bar{\bar{I}} + \frac{i}{\omega\epsilon_0} \bar{\bar{\sigma}} \right) \vec{E} = 0 \tag{2.32}$$

or written in terms of the dielectric tensor $\bar{\bar{\epsilon}} = \bar{\bar{I}} + \frac{i}{\omega\epsilon_0}\bar{\bar{\sigma}}$ (with $\bar{\bar{I}}$ being the identity tensor),

$$\vec{k} \times \left(\vec{k} \times \vec{E} \right) + \frac{\omega^2}{c^2} \bar{\bar{\epsilon}} \vec{E} = 0. \tag{2.33}$$

Defining the refractive index from optics $N = \frac{c}{v}$, where $\vec{v}$ is the phase velocity, $\vec{v}_p = \frac{\omega}{\vec{k}}$, thus the refractive index $\vec{N}$ is

$$\vec{N} = \frac{\vec{k}c}{\omega}. \tag{2.34}$$

Substituting into the equation and noting that c and ω are just scalars, we get

$$\vec{N} \times \left(\vec{N} \times \vec{E} \right) + \bar{\bar{\epsilon}} \vec{E} = 0. \tag{2.35}$$

Through the equation of motion (2.10) and the small amplitude 1st-order perturbations the elements of the dielectric tensor are derived in [3] and [12]. The dielectric tensor is defined as such:

$$\bar{\bar{\epsilon}} = \begin{bmatrix} S & -iD & 0 \\ iD & S & 0 \\ 0 & 0 & P \end{bmatrix}, \tag{2.36}$$

where the matrix elements in Stix (1962) notation are

$$S = 1 - \sum_\sigma \frac{\omega_{p\sigma}^2}{\omega^2 - \omega_{c\sigma}^2}, \quad D = \sum_\sigma \frac{\omega_{c\sigma}}{\omega} \frac{\omega_{p\sigma}^2}{\omega^2 - \omega_{c\sigma}^2}, \quad P = 1 - \sum_\sigma \frac{\omega_{p\sigma}^2}{\omega^2}. \tag{2.37}$$

The dispersion relations for cold plasma waves appear from this formulation. Since the electron- and ion cyclotron resonance frequencies (ECR and ICR) vary from each other by 3 orders of magnitude with ECR being the greater, and we are interested in the electron cyclotron resonances, the ions will be mostly ignored going on. Introducing the normalized notation $X = \omega_{pe}^2/\omega^2$ and $Y = \omega_{ce}/\omega$ and dropping the ions, the Stix notation then compactly becomes

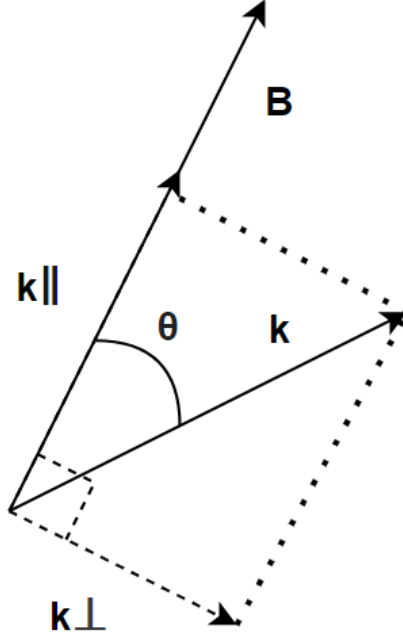$$S = 1 - \frac{X}{1 - Y^2}, \quad D = \frac{Y X}{1 - Y^2}, \quad P = 1 - X. \tag{2.38}$$

8

Figure 3: Scetch of the magnetic field vector and $\vec{k}$ at the angle θ to one another. $\vec{k}$ is often split into it's components parallel and perpendicular to $\vec{B}$ as seen in the figure.

2.3.1 Wave Modes, Resonances and Cutoffs

Now with the dielectric tensor $\bar{\bar{\epsilon}}$ and the refractive index $\vec{N}$ defined, the next step is to look for solutions to equation (2.35). Often the wave vector $\vec{k}$ is be split into it's parallel and perpendicular components vs. the magnetic field $\vec{B}$ separated by the angle θ as seen in Fig. 3. There is only one parallel component of $\vec{k}$ to $\vec{B}$, which can go either same or opposite direction of $\vec{B}$, while there are infinitely many perpendicular components found by rotating $\vec{k}$ around $\vec{B}$. The magnetic field will generally point in the toroidal direction following the torus as seen in Fig. 1. Noting that the components of the refractive index vector rely directly on the wavevector components as c and ω are scalars, the coordinate system is defined so the refractive index vector only has an x- and z-component as in [3][4][12], where the x-axis is per definition perpendicular to the z-axis, and the magnetic field is only in the z-direction, thus as in Fig. 3 the x-component becomes the perpendicular component $N_x = N_\perp = N \sin\theta$, the y-copmponent $N_y = 0$ and the z-component becomes the parallel component $N_z = N_\parallel = N \cos\theta$ all with $N^2 = N_x^2 + N_y^2 + N_z^2 = N_\perp^2 + N_\parallel^2$, so that (2.35) becomes

$$\begin{bmatrix} S - N^2\cos^2\theta & -iD & N^2\sin\theta\cos\theta \\ iD & S - N^2 & 0 \\ N^2\sin\theta\cos\theta & 0 & P - N^2\sin^2\theta \end{bmatrix} \cdot \begin{bmatrix} E_x \\ E_y \\ E_z \end{bmatrix} = 0, \tag{2.39}$$

where θ is denoted as the angle between the wavevector $\vec{k}$ and the magnetic field $\vec{B}$. Wanting to exclude trivial solutions where everything is 0, Cramer's rule is applied [1], where solutions to the system are found by setting the determinant to 0,

$$\mathcal{D}_{cold} = (S - N^2\cos^2\theta)(S - N^2)(P - N^2\sin^2\theta) - D^2(P - N^2\sin^2\theta) - (N^2\sin\theta\cos\theta)^2(S - N^2) = 0. \tag{2.40}$$

To find simple solutions, the angle θ is first set to $\theta = 0$, then $\theta = \pi/2$ and then any arbitrary angle. Two instantly determinable solutions arrive by setting $\theta = 0$, as the two tensor elements with $N^2\sin\theta\cos\theta = 0$ at both $\theta = 0$ and $\theta = \pi/2$, resulting in the dispersion relation for $\theta = 0$:

$$\mathcal{D}_{\theta=0}(\omega, \vec{k}) = \pm D + S - N^2 = 0, \tag{2.41}$$

9

giving the left and right polarized wave modes,

$$R = S + D, \quad L = S - D. \tag{2.42}$$

For an angle $\theta = \pi/2$ the determinant gives the dispersion relation

$$\mathcal{D}_{\theta=\pi/2}(\omega, \vec{k}) = \left[S(S - N^2) - D^2 \right] (P - N^2) = 0. \tag{2.43}$$

For an arbitrary angle θ we get the O- and X-modes (ordinary and extraordinary), which cast into the Appleton-Hartree formulation is [12]

$$\mathcal{D}_{App}(\omega, \vec{k}) = 1 - \frac{k^2 c^2}{\omega^2} - \frac{2X(1 - X)}{2(1 - X) - Y^2 \sin^2 \theta \pm \Gamma}, \tag{2.44}$$

where $\Gamma = \left[Y^4 \sin^4 \theta + 4Y^2(1 - X)^2 \cos^2 \theta \right]^{\frac{1}{2}}$ and the normalized parameters X and Y are defined as $X = \omega_{pe}^2/\omega^2$ and $Y = \omega_{ce}/\omega$, dropping the ion frequencies. The $\pm$ sign determines if it is an ordinary or extraordinary mode. Specifically the O-mode arises as

$$\mathcal{D}_O(\omega, \vec{k}) = 1 - X - \frac{c^2 k^2}{\omega^2} = P - N^2 = 0 \tag{2.45}$$

and X-mode as

$$\mathcal{D}_X(\omega, \vec{k}) = 1 - \frac{X(1 - X)}{1 - X - Y^2} - \frac{c^2 k^2}{\omega^2} = 0. \tag{2.46}$$

In order to characterize the wave modes in the cold plasma we will be looking for resonances and cutoffs. Resonances occur when the index of refraction explodes, $N^2 \to \infty$, and cutoffs occur when it diminishes, $N^2 = 0$, corresponding to a reflection of the wave. Analyzing the limits, we have the principle resonances, where N^2 has a resonance at either $\theta = 0$ or $\theta = \pi/2$, thus at $R \to \infty$, $L \to \infty$ and $S = 0$, corresponding to the electron cyclotron resonance, the ion cyclotron resonance and the upper and lower hybrid resonances respectively [3][4][12]. The electron cyclotron resonance occurs when $\omega_{ce} = \omega$ since the denominator goes to 0,

$$R = S + D = 1 + \left(\frac{\omega_{ce}}{\omega} - 1 \right) \frac{\omega_{pe}^2}{\omega^2 - \omega_{ce}^2} \to \infty \text{ for } \omega_{ce} \to \omega \tag{2.47}$$

The upper hybrid resonance ω_{UH} is

$$S = 1 - \frac{\omega_{pe}^2}{\omega^2 - \omega_{ce}^2} = 0 \iff \omega_{UH}^2 = \omega_{pe}^2 + \omega_{ce}^2 = \omega^2, \tag{2.48}$$

and the lower hybrid resonance ω_{LH} is

$$\omega_{LH} = \omega_{ce} \omega_{ci} \left(\frac{\omega_{pe}^2 + \omega_{ce} \omega_{ci}}{\omega_{ce}^2 + \omega_{ci}^2} \right). \tag{2.49}$$

Cutoffs are at directly found from $\theta = 0$ at $R = 0$ and $L = 0$, while a cutoff at $P = 0$ is found by the dispersion relation for the ordinary mode [3]. Often O-mode and X-mode are used for beam injection into the plasma, since they propagate perpendicular to the magnetic field, which is mainly toroidal. For all waves, the density structure of a plasma yields consequences for heating techniques, since wave heating schemes include injecting O-mode and X-mode beams, where for one thing, O-mode waves cannot propagate beyond the $P = 0$ cutoff, meaning at $\omega_p^2 = \frac{n_e q^2}{\epsilon_0 m_e} > \omega^2$.
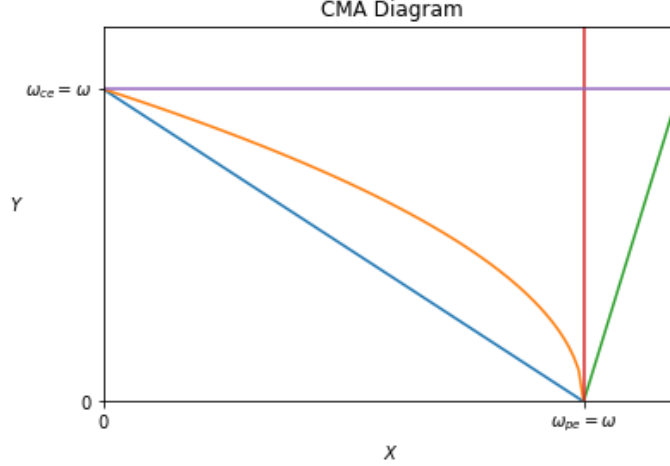
Figure 4: CMA Diagram showing the cutoffs and resonances of wave modes arising from the cold plasma approximation. Blue is the $R = 0$ cutoff, orange the upper hybrid resonance, purple the electron cyclotron resonance, red the $P = 0$ cutoff and green the $L = 0$ cutoff. The axes are normalized to by the wave frequency ω, $X = \omega_p^2/\omega^2$ and $Y = \omega_c/\omega$, which compactly highlights the propagation regimes for the different waves in a cold plasma.

2.3.2 CMA Diagram

A good visualization of the propagation regimes including the resonances and cutoffs is the CMA diagram. Normally the axes would extend to include the mass fraction m_i/m_e, but we are only interested in the area about $X = [0, 2]$ and $Y = [0, 2]$, since it includes the electron cyclotron resonances, which are used for ECRH plasma heating. A snippet of the CMA diagram around the electron cyclotron resonance can be seen in Fig. 4. For the cold electromagnetic waves, O-mode waves propagate only on the left side of $P = 0$ cutoff (red), X-mode below the lower hybrid $R = 0$ cutoff (blue) or above the upper hybrid resonance (orange) and on the left side of the $L = 0$ cutoff (green). The $L = 0$ and $R = 0$ cutoffs and their respective resonances also display the propagation limits of R- and L-mode waves.

2.4 Kinetic Plasma and Bernstein Waves

Having considered the cold plasma waves, we now dig into the electrostatic waves, particularly the electron Bernstein waves (EBW). As the phase velocity of an EBW is in proximity to the thermal velocity, thus the dispersion relation for the waves requires a kinetic treatment. EBW do not appear from fluid or magneto-hydro-dynamic approaches to plasma like the cold plasma waves. Bernstein waves are electrostatic waves, that at harmonics of the cyclotron frequency propagate perpendicular to $\vec{B}_0$. Electron Bernstein waves and other electrostatic waves propagate in finite plasmas with phase velocities v considerably small compared to the speed of light c, hence the electrical field can be expressed by $\vec{E} = -\vec{\nabla}V$ with V being the electrostatic potential. Using Poisson's equation in a similar approach to obtaining the cold plasma dielectric tensor an expression for the electric susceptibility $\mathcal{X}(\vec{k}, \omega)$, which is related to the dielectric tensor by $\mathcal{X} = \bar{\bar{1}} + \bar{\bar{\epsilon}}$, is found in [7] (the full expression is in 7.1) leading to the complex dispersion relation,

$$\mathcal{D}_{kin}\left(\vec{k}, \omega\right) = l_{Te}^2 k_\perp^4 + S k_\perp^2 + P k_\parallel^2 - \frac{\omega^2}{c^2}\left(S^2 - D^2\right) + iI = 0. \tag{2.50}$$

The resulting dispersion relation describes the merger of EBW and slow X-mode waves at the upper hybrid resonance. The imaginary part of the dispersion relation can roughly be ignored in an ideal
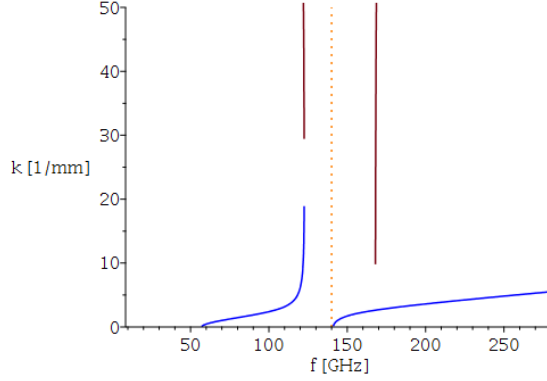
11

Figure 5: The figure depicts the wavenumber k vs. the frequency of an injected wave for X-mode (blue) and EBWs (red). The electron density is here constant at $n_e = 10^{20}\,\mathrm{m^{-3}}$, and the chosen injection frequency is shown as the yellow dotted line at $f = 140\,\mathrm{GHz}$ with $\theta = \pi/2$, constant magnetic field $B = 3\,\mathrm{T}$ and constant temperature $T_e = 10\,\mathrm{eV}$.

system as it handles damping of the waves due to electron collisions, resulting in the dispersion relation

$$\mathcal{D}_{kin}\left(\vec{k}, \omega\right) = l_{Te}^2 k_\perp^4 + S k_\perp^2 + P k_\parallel^2 - \frac{\omega^2}{c^2}\left(S^2 - D^2\right) = 0 \tag{2.51}$$

where

$$l_{Te}^2 = \frac{3\omega_{pe}^2 \omega_{ce}^2}{\left(4\omega_{ce}^2 - \omega^2\right)\left(\omega^2 - \omega_{ce}^2\right)} r_{Le}^2 \tag{2.52}$$

and the larmor radius and thermal velocity are

$$r_{Le}^2 = \frac{\nu_{Te}^2}{2\omega_{ce}^2} = \frac{m_e T_e}{e^2 B^2}, \quad \nu_{Te} = \sqrt{\frac{2T_e}{m_e}}, \tag{2.53}$$

and by using the normalization notation as in the cold plasma approximation, $X = \omega_{pe}^2/\omega^2$ and $Y = \omega_c/\omega$, l_{Te}^2 becomes

$$l_{Te}^2 = \frac{3X T_e}{m_e \omega^2 \left(4Y^2 - 1\right)\left(1 - Y^2\right)}. \tag{2.54}$$

Rewriting (2.51) using $\vec{k}_\perp = k \sin\theta$ and $\vec{k}_\parallel = k \cos\theta$:

$$\mathcal{D}_{kin}\left(\vec{k}, \omega\right) = k^4 l_{Te}^2 \sin^4\theta + k^2 \left(S \sin^2\theta + P \cos^2\theta\right) - \frac{\omega^2}{c^2}\left(S^2 - D^2\right) = 0. \tag{2.55}$$

The dispersion relation is bi-quadratic, thus can be solved using the quadratic formula for $x = k^2$,

$$k^2 = -\frac{\left(S \sin^2\theta + P \cos^2\theta\right) \pm \sqrt{\left(S \sin^2\theta + P \cos^2\theta\right)^2 - 4 l_{Te}^2 \sin^4\theta \left(-\frac{\omega^2}{c^2}\left(S^2 - D^2\right)\right)}}{2 l_{Te}^2 \sin^4\theta}. \tag{2.56}$$

In Fig. 5 the wavenumbers k for X-mode and EBWs are plotted vs input frequency $f = \omega/2\pi$ for specific values of n_e, B and T_e. Here we see the two $\pm$ branches of the solution for k in (2.56) and the corresponding frequency where there is no corresponding propagation. Electron Bernstein waves are used to heat plasma at the electron cyclotron resonance or its harmonics. In Fig. 6 a sketch of a O-X-EBW (black-cyan-yellow) conversion heating scheme is visualized in the CMA diagram. This heating scheme utilizes the propagation areas, where it is natural to start a wave from the outside at $n_e = 0 \rightarrow X = 0$, where EBW cannot on its own reach the electron cyclotron resonance (ECR) in order for ECRH to occur. ECRH is possible on the left and right side of $X = 1$, but has to be to the left of the $L = 0$ cutoff (green). The simulated conversion from X-mode to electron Bernstein is possible thanks to the dispersion relation (2.51) being able to describe both slow X-mode waves and EBW at the upper hybrid resonance where the conversion will take place.
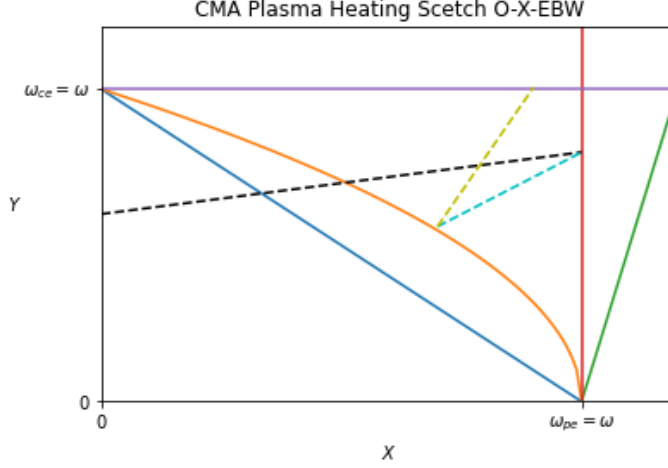
12

Figure 6: Sketch of electron cyclotron resonance heating (ECRH) scheme, where an injected O-mode (black) wave is converted to X-mode (cyan) at $P = 0$ (red), then at the upper hybrid resonance (orange) is converted to EBW (yellow), utilizing an ECRH scheme. Further explanation of the CMA diagram can be found in Fig. 4.

2.5 Three Wave Interactions and Parametric Decay Instabilities

Parametric decay instabilities (PDI) refers to a collection of nonlinear processes including a transfer of energy between waves. Using an X-mode wave pump, and by conservation of energy and momentum:

$$\omega_0 = \omega_1 + \omega_2, \quad \omega_0 + \omega_1 = \omega_3. \tag{2.57}$$

$$\vec{k}_0 = \vec{k}_1 + \vec{k}_2, \quad \vec{k}_0 + \vec{k}_1 = \vec{k}_3. \tag{2.58}$$

The first equation relates to the decay of a wave with frequency ω_0 and wave vector $\vec{k}_0$ into daughter waves with frequencies ω_1 and ω_2 and wave vectors $\vec{k}_1$ and $\vec{k}_2$. The same relation holds for a new pump wave of ω_0 and $\vec{k}_0$ added to one of the former daughter waves, thus collecting in a new wave of ω_3 and $\vec{k}_3$ [13][14].

2.6 Ray Tracing

The dispersion relations found in the previous sections are studied through geometric optics, and the next step is to determine the dispersion dependence of $\vec{k}$ and $\vec{r}$. Given the dispersion relation

$$\mathcal{D}(\vec{k}, \vec{r}) = 0, \tag{2.59}$$

and noting that any arbitrary nearby position $\vec{r} + \delta\vec{r}$ also satisfies the dispersion relation,

$$\mathcal{D}(\vec{k} + \delta\vec{k}, \vec{r} + \delta\vec{r}) = 0, \tag{2.60}$$

or as the first order Taylor expansion around $\vec{k} + \delta\vec{k}$ and $\vec{r} + \delta\vec{r}$,

$$\delta\vec{k}\frac{\partial\mathcal{D}}{\partial\vec{k}} + \delta\vec{r}\frac{\partial\mathcal{D}}{\partial\vec{r}} = 0, \tag{2.61}$$

the dispersion relation with respect to $\vec{k}$ and $\vec{r}$ can be written in terms of some time or ray length, δs. Using the chain rule to change the derivative to s, the dispersion relation can be solved by the two coupled equations in the form,

$$\frac{d\vec{k}}{ds} = -\frac{\partial\mathcal{D}}{\partial\vec{r}}, \quad \frac{d\vec{r}}{ds} = \frac{\partial\mathcal{D}}{\partial\vec{k}}. \tag{2.62}$$

13

Here, $\mathcal{D}$ plays the role of the Hamiltonian. The formulation of the ray tracing equations used in this project is from [12] in the form

$$\frac{d\vec{r}}{ds} = -\text{sgn}\left(\frac{\partial \mathcal{D}}{\partial \omega}\right) \frac{\vec{\nabla}_k \mathcal{D}}{|\vec{\nabla}_k \mathcal{D}|}, \tag{2.63}$$

$$\frac{d\vec{k}}{ds} = \text{sgn}\left(\frac{\partial \mathcal{D}}{\partial \omega}\right) \frac{\vec{\nabla}_r \mathcal{D}}{|\vec{\nabla}_k \mathcal{D}|}, \tag{2.64}$$

where the angular frequency dependence is added, and the ray is normalized with respect to the length of $\vec{\nabla}_k \mathcal{D}$. sgn(x) corresponds to a function taking the sign of x; if x is positive, negative or 0, then the sign function will return respectively $+1$, -1 or 0. A similar derivation can be found in [3]. Ray tracing only works if the geometrical optics assumptions are correct. In geometric optics the propagation medium is assumed nearly homogeneous, which is ideally the case for the wavelength $\lambda_0 \to 0$ [11]. This is the case for larger tokamaks utilizing high frequencies, and in our case microwaves at a frequency of 140 GHz corresponding to a wavelength of $\lambda_0 = 2.1$ mm, which is small compared to the size of even a small fusion reactor. Geometric optics is fitting for propagation through a homogeneous material, but also works for material where changes are very small or non-existent in the local scope, thus small enough step sizes of a ray tracer would yield fitting results.

3 Ray Tracing in an Artificial Tokamak

As mentioned earlier, ray tracing presents a cost efficient method of numerical simulation of waves propagating through a plasma. In this thesis a ray tracer is written in C++ to trace both O-, X-mode and electron Bernstein waves for general purpose of both heating schemes and diagnostics of plasma using microwave technology: First using the Appleton-Hartree dispersion relation (2.44) for O- and X-mode waves and then the kinetic EBW/slow X-mode dispersion relation (2.51) for EBW and X-mode waves at the upper hybrid resonance in ideal conditions of zero damping and a magnetic field in the toroidal direction. The scripts are on Github at `https://github.com/s183753/Bachelor-Thesis_Scripts`. For this project, the magnetic fields are assumed to be completely toroidal, even though to keep the plasma contained, the magnetic fields spiral around the tokamak as seen with the black field lines in Fig. 1.
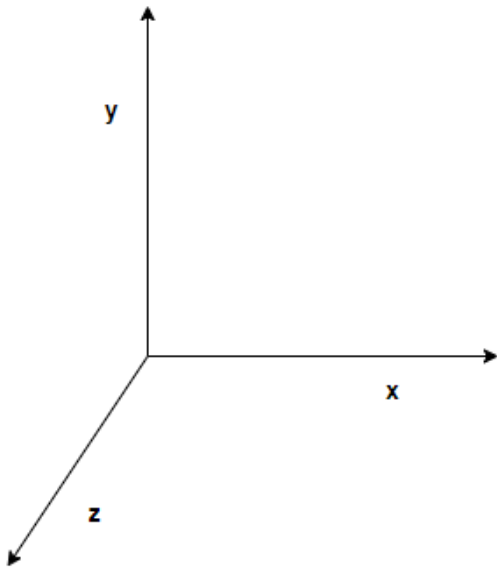
Figure 7: Defined Cartesian coordinate system. All calculations are done in Cartesian coordinates, and a conversion to cylindrical coordinates is made when fetching grid values of the parameters n_e, B and T_e. During conversion from Cartesian to cylindrical coordinates $y \to Z$, $\sqrt{x^2 + z^2} \to R$
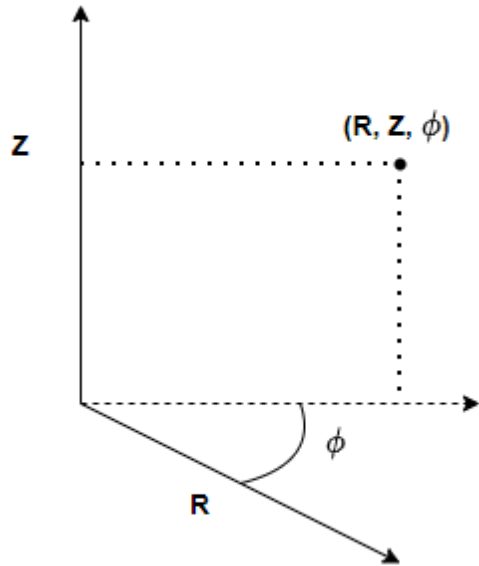
Figure 8: Defined cylindrical coordinate system. The grids are kept in cylindrical coordinates, while the majority of the simulations are done in Cartesian coordinates.

3.1 Grid Definitions

Grids of the electron density n_e, magnetic field B and temperature T are normally found experimentally. These parameters are what can vary throughout a plasma and have a great impact on how the plasma and waves in it behave. For this project symmetry in the toroidal direction is assumed in order to establish a simple electron density, magnetic field and temperature data structure. This lead to the use of cylindrical coordinates, even though most of the C++ code is written to use Cartesian coordinates. Here using cylindrical coordinates $\vec{r} = (R, Z, \phi)$ allows a data set for each grid to consist of a 2D matrix instead of a 3D, allowing for simpler parameter distributions. The grids consist of 100×100-matrices. Inspiration for the parameters is taken from experiments done on MAST Upgrade (Mega Ampere Spherical Tokamak) in England to get a realistic approximation

[15]. As the simulation progresses, the position- and wave-vectors are updated all using Cartesian coordinates ($\vec{r} = (x, y, z)$ and $\vec{k} = (k_x, k_y, k_z)$). In order to get the appropriate parameters n_e, B and T_e from their respective grids, a conversion from Cartesian coordinates to cylindrical coordinates is made. The defined Cartesian coordinate system can be seen in Fig. 7. A coordinate conversion consists of letting the x and z components become the radius component, $R = \sqrt{x^2 + z^2}$, and the y component directly translate to the vertical Z component, $Z = y$. ϕ is thus the toroidal angle (the angle around the torus). The defined cylindrical coordinate system can be seen in Fig. 8.

The torus is defined to have an outer ring border at a radius of $R = 5$ m and an inner ring border at $R = 2$ m. Perfectly circular cross sections of the torus are also assumed for simplicity, although tokamaks are often taller than they are wide. Using cylindrical coordinates to describe the cross sections, the center of a cross section is defined to be at $Z = 0$ m, where Z inside the torus spans from $Z = [-1.5, 1.5]$ m. The electron density and temperature grids are crafted as Gaussian distributions with peaks at the middle of the torus cross section at $(R, Z) = (3.5\,\text{m}, 0\,\text{m})$. The two grids have the same distributions since the electron densities and temperatures are strongly correlated. The peaks of the distributions are at $n_e = 10^{20}\,\text{m}^{-3}$ and $T_e = 10\,\text{eV}$ for the electron densities and temperatures respectively.

Measured in Tesla, the magnetic field strength varies as $B \propto 1/R$, where R is the radius from the center of the tokamak. The radius spans from $R = 2$ m to $R = 5$ m, thus a possible singularity at $R = 0$ is ignored. The proportionality value for the magnetic field strength is chosen so the electron cyclotron resonance (ECR) is in the center of the cross-section of the tokamak ring, thus at $R = 3.5$ m and $Z = 0$ m, with a value of $\omega = \omega_c = eB(3.5)/m_e \iff B(3.5) = m_e\omega/e \approx 5\,\text{T}$. The magnetic field strength is tunable through the electric circuitry surrounding the tokamak. The used injection frequency is $f = 140\,\text{GHz}$, thus $\omega = 2\pi 140\,\text{GHz}$.

3.2 Ray Tracing and Finite Difference Method

Starting by the coupled ray equations (2.63) and (2.64) the waves propagating through a plasma can be followed by a ray tracer. The ray tracer uses numerical differentiation at small enough time steps (or ray length steps in our case) ds and for a large enough quantity of iterations N in order to visualize the propagation of the different modes and for the method to be a close enough approximation. This relies heavily on a numerical method; in this case the Finite Difference Method [2] using the forward difference quotient with ray length steps ds,

$$\frac{\partial f(s)}{\partial s} = \frac{f(s + ds) - f(s)}{ds} + \mathcal{O}(ds), \tag{3.1}$$

and the central difference quotient for finding the gradients of the grid parameters,

$$\frac{\partial f(x)}{\partial x} = \frac{f(x + \delta x) - f(x - \delta x)}{2\delta x} + \mathcal{O}(\delta x^2). \tag{3.2}$$

The central difference quotient yields a better approximation than both forward or backwards with an error of $\mathcal{O}(\delta^2)$ for central difference compared to $\mathcal{O}(\delta)$ for forward difference. A problem worth noting is the central difference quotient relies on a having a value x, where you can afford to take a step of δ in both directions. This of course does not work when you are on the edge of the grid, as there are no points further out than the one currently in use. Edge handling in this simulation is done by checking if the grid coordinates about to be used are lower than 0 or higher than the number of grid points in said direction, thus being out of the grid scope. If either occurs, the grid coordinates are set to being on the nearest edge in that dimension. Another solution could be to interpolate a fictitious point outside the edge by taking the gradient using the grid edge point and one further into the grid, but deviations in the edge grid values and the gradient interpolation are so small that it will not make a noticeable difference.

The Appleton-Hartree formulation (2.44) is used to trace the rays of O- and X-mode from the cold

plasma approximation, though the Appleton-Hartree formulation has trouble describing the X-mode wave around the upper hybrid resonance. Appleton-Hartree works for any angle of propagation to the magnetic field, whereas the kinetic dispersion relation for Bernstein waves are derived under the assumption of perpendicular propagation to the magnetic field. Again noting the simulated changes in parameters in the tokamak are considerably large compared to the $\approx 2.1\,\text{mm}$ wavelength of the used microwaves gives us the confidence to proceed with simulations using ray tracing.

3.2.1 Appleton-Hartree, O- and X-mode Waves

To initialize the simulation, a start wavenumber k is found by calculating the theoretical wavenumber. Here the corresponding dispersion relation is solved for k, and then k is calculated for the given position. The gradient of a function corresponds to differentiation of a function in all directions of a vector. The spatial gradient with respect to $\vec{r}$ using the help function $f(\vec{r})$ with $\vec{r} = (x, y, z)$ being the position vector is then the operator

$$\vec{\nabla}_r f(\vec{r}) = \left(\frac{\partial}{\partial x} f(x, y, z), \frac{\partial}{\partial y} f(x, y, z), \frac{\partial}{\partial z} f(x, y, z) \right). \tag{3.3}$$

For the Appleton-Hartree dispersion relation a convenient formulation relying on the unit vectors of the wave vector and toroidal angle is derived in [12]:

$$\frac{d\vec{r}}{ds} = -\text{sgn}\left(\frac{\partial \mathcal{D}}{\partial \omega} \right) \frac{\frac{\partial \mathcal{D}}{\partial k} \vec{e}_k + \frac{1}{k} \frac{\partial \mathcal{D}}{\partial \theta} \vec{e}_\theta}{\left[\left(\frac{\partial \mathcal{D}}{\partial k} \right)^2 + \left(\frac{1}{k} \frac{\partial \mathcal{D}}{\partial \theta} \right)^2 \right]^{\frac{1}{2}}}, \tag{3.4}$$

$$\frac{d\vec{k}}{ds} = \text{sgn}\left(\frac{\partial \mathcal{D}}{\partial \omega} \right) \frac{\frac{\partial \mathcal{D}}{\partial X} \vec{\nabla}_r X + \frac{\partial \mathcal{D}}{\partial Y^2} \vec{\nabla}_r Y^2 + \frac{\partial \mathcal{D}}{\partial \theta} \vec{\nabla}_r \theta}{\left[\left(\frac{\partial \mathcal{D}}{\partial k} \right)^2 + \left(\frac{1}{k} \frac{\partial \mathcal{D}}{\partial \theta} \right)^2 \right]^{\frac{1}{2}}}, \tag{3.5}$$

where the unit vectors are found by

$$\vec{e}_k = \vec{k}/k, \quad \vec{e}_\theta = \frac{\vec{k} \times \left(\vec{k} \times \vec{B} \right)}{|\vec{k} \times \vec{k} \times \vec{B}|}, \tag{3.6}$$

using the same normalizing notation as in the Cold Plasma section,

$$X = \frac{\omega_{pe}^2}{\omega^2}, \quad Y = \frac{\omega_{ce}}{\omega}, \tag{3.7}$$

which for the Stix notation is

$$P = 1 - X, \quad S = 1 - \frac{X}{1 - Y^2}, \quad D = \frac{YX}{1 - Y^2}. \tag{3.8}$$

In the code the following functions for calculating the gradients based on [12] are used:

$$A(X) = 2X(1 - X), \quad B_m(X, Y^2, \theta) = 2(1 - X) - Y^2 \sin^2 \theta + m\Gamma, \quad G = \frac{A}{B_m}, \tag{3.9}$$

with $m = \pm 1$ where $m = 1$ is for ordinary mode and $m = -1$ for extraordinary mode. This results in the Appleton-Hartree dispersion relation in current notation,

$$\mathcal{D}_{App}(k, \theta, X, Y^2, \omega) = 1 - \frac{k^2 c^2}{\omega^2} - G, \tag{3.10}$$

resulting in the derivatives:

$$\frac{\partial \mathcal{D}_{App}}{\partial k} = -\frac{2kc^2}{\omega^2}, \tag{3.11}$$

$$\frac{\partial \mathcal{D}_{App}}{\partial \theta} = \frac{A}{B_m^2} \frac{\partial B_m}{\partial \theta} = -G \frac{2 \sin \theta \cos \theta}{B_m} Y^2 \left[1 - m \frac{Y^2 \sin^2 \theta - 2(1-X)^2}{\Gamma} \right], \tag{3.12}$$

$$\frac{\partial \mathcal{D}_{App}}{\partial X} = -\frac{\partial G}{\partial X} - \frac{\partial G}{\partial \Gamma} \frac{\partial \Gamma}{\partial X}, \quad \frac{\partial \mathcal{D}_{App}}{\partial Y^2} = -\frac{\partial G}{\partial Y^2} - \frac{\partial G}{\partial \Gamma} \frac{\partial \Gamma}{\partial Y^2}, \tag{3.13}$$

$$\frac{\partial G}{\partial X} + \frac{\partial G}{\partial \Gamma} \frac{\partial \Gamma}{\partial X} = \frac{1}{B_m^2} \left[2(1-2X)B_m + 2A + mA \frac{4Y^2(1-X)}{\Gamma} \cos^2 \theta \right], \tag{3.14}$$

$$\frac{\partial G}{\partial Y^2} + \frac{\partial G}{\partial \Gamma} \frac{\partial \Gamma}{\partial Y^2} = \frac{A}{B_m^2} \left[\sin^2 \theta - m \frac{Y^2 \sin^4 \theta + 2(1-X)^2 \cos^2 \theta}{\Gamma} \right], \tag{3.15}$$

$$\frac{\partial \mathcal{D}_{App}}{\partial \omega} = \frac{2k^2 c^2}{\omega^3} + \frac{2X}{\omega} \left(\frac{\partial G}{\partial X} + \frac{\partial G}{\partial \Gamma} \frac{\partial \Gamma}{\partial X} \right) + \frac{2Y^2}{\omega} \left(\frac{\partial G}{\partial Y^2} + \frac{\partial G}{\partial \Gamma} \frac{\partial \Gamma}{\partial Y^2} \right), \tag{3.16}$$

and with the gradients depending on the grids

$$\vec{\nabla}_r X = X \frac{\vec{\nabla}_r n_e}{n_e}, \quad \vec{\nabla}_r Y^2 = 2Y^2 \frac{\vec{\nabla}_r B}{B}, \tag{3.17}$$

and

$$\vec{\nabla}_r \theta = -\frac{1}{k \sin \theta} \vec{\nabla}_r \left(\vec{k} \cdot \frac{\vec{B}}{B} \right), \tag{3.18}$$

with the gradient only acting on the magnetic field in the last equation.

3.2.2   X-mode and Bernstein Waves near the UHR

Returning to the notation shown in (2.63) and (2.64),

$$\frac{d\vec{r}}{ds} = -\text{sgn} \left(\frac{\partial \mathcal{D}}{\partial \omega} \right) \frac{\vec{\nabla}_k \mathcal{D}}{|\vec{\nabla}_k \mathcal{D}|}, \tag{3.19}$$

$$\frac{d\vec{k}}{ds} = \text{sgn} \left(\frac{\partial \mathcal{D}}{\partial \omega} \right) \frac{\vec{\nabla}_r \mathcal{D}}{|\vec{\nabla}_k \mathcal{D}|}, \tag{3.20}$$

and reciting the kinetic dispersion relation (2.51) merging the slow X-mode waves and EBW:

$$\mathcal{D}_{kin} \left(\vec{k}, \omega \right) = k^4 l_{Te}^2 \sin^4 \theta + k^2 \left(S \sin^2 \theta + P \cos^2 \theta \right) - \frac{\omega^2}{c^2} \left(S^2 - D^2 \right) = 0, \tag{3.21}$$

where the gradients with respect r and k of the dispersion relation are now found. Starting by determining what is constant and what is dependent on $\vec{r}$ and $\vec{k}$ by noting that $\vec{k}$ is explicit in the expression, while $\vec{r}$ is implicit in the functions $l_{Te}^2(\vec{r})$, $S(\vec{r})$, $P(\vec{r})$, $S^2(\vec{r})$ and $D^2(\vec{r})$. First taking the gradient with respect to $\vec{k}$,

$$\vec{\nabla}_k \mathcal{D}_{kin} \left(\vec{k}, \omega \right) = \begin{pmatrix} 4k_x k^2 l_{Te}^2 \sin^4 \theta + 2k_x \left(S \sin^2 \theta + P \cos^2 \theta \right) \\ 4k_y k^2 l_{Te}^2 \sin^4 \theta + 2k_y \left(S \sin^2 \theta + P \cos^2 \theta \right) \\ 4k_z k^2 l_{Te}^2 \sin^4 \theta + 2k_z \left(S \sin^2 \theta + P \cos^2 \theta \right) \end{pmatrix}, \tag{3.22}$$

and now the gradient with respect to $\vec{r}$,

$$\vec{\nabla}_r \mathcal{D}_{kin} \left(\vec{k}, \omega \right) = k^4 \vec{\nabla}_r \left(l_{Te}^2 \right) \sin^4 \theta + k^2 \left(\vec{\nabla}_r S \sin^2 \theta + \vec{\nabla}_r P \cos^2 \theta \right) - \frac{\omega^2}{c^2} \left(\vec{\nabla}_r \left(S^2 \right) - \vec{\nabla}_r \left(D^2 \right) \right) \tag{3.23}$$
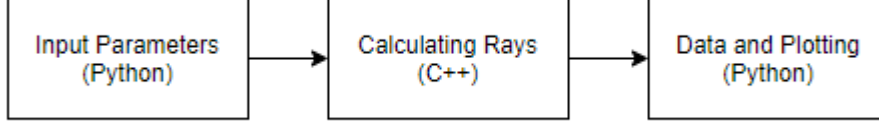
Figure 9: Flowchart illustrating the data flow from input in Python to C++, where all the calculating and grids are done, then back to Python for visualization and data output.

The expressions are written in the same normalized combined with Stix notation as in the Appleton-Hartree formulation with $X = \omega_{pe}^2/\omega^2$ and $Y = \omega_{ce}/\omega$. $P, S, D, \vec{\nabla}_r X$ and $\vec{\nabla}_r Y^2$ are the same as for Appleton-Hartree, adding to the list:

$$l_{Te}^2 = \frac{3XT_e}{m_e\omega^2\left(4Y^2 - 1\right)\left(1 - Y^2\right)}, \tag{3.24}$$

$$\vec{\nabla}_r l_{Te}^2 = \frac{3}{m_e\omega^2}\left[\frac{\left(\vec{\nabla}_r X T_e + X\vec{\nabla}_r T_e\right)}{(4Y^2 - 1)(1 - Y^2)} - \frac{T_e X(5\vec{\nabla}_r Y^2 - 4\vec{\nabla}_r Y^4)}{(5Y^2 - 4Y^4 - 1)^2}\right], \tag{3.25}$$

$$\vec{\nabla}_r Y^4 = 4Y^4\frac{\vec{\nabla}_r B}{B}, \tag{3.26}$$

$$\vec{\nabla}_r P = -\vec{\nabla}_r X, \tag{3.27}$$

$$\vec{\nabla}_r S = -\frac{\vec{\nabla}_r X}{1 - Y^2} - \frac{X\vec{\nabla}_r Y^2}{(1 - Y^2)^2}, \tag{3.28}$$

$$\vec{\nabla}_r D = -\vec{\nabla}_r SY + \frac{X\vec{\nabla}_r Y}{1 - Y^2}, \tag{3.29}$$

$$\vec{\nabla}_r D^2 = 2D\vec{\nabla}_r D, \quad \vec{\nabla}_r S^2 = 2S\vec{\nabla}_r S, \tag{3.30}$$

$$\frac{\partial \mathcal{D}_{kin}}{\partial \omega} = k^4\sin^4\theta\frac{\partial l_{Te}^2}{\partial \omega} + k^2\left(\frac{\partial S}{\partial \omega}\sin^2\theta + \frac{\partial P}{\partial \omega}\cos^2\theta\right) - 2\frac{\omega}{c^2}\left(S^2 - D^2\right) - \frac{\omega^2}{c^2}\left(\frac{\partial S^2}{\partial \omega} - \frac{\partial D^2}{\partial \omega}\right) = 0 \tag{3.31}$$

3.3 Script Layout

Ray tracing is more cost efficient than full wave simulations. Even so, there is a risk of lacking precision if the time steps are not small enough. C++ is chosen as main programming language due to its generally low run time compared to higher level languages such as Python or MATLAB in anticipation of large run times during simulation. C++ does however lack easy visualization methods as the two other, so Python is chosen to support with the data analysis and plotting. The general flow of information between the languages is depicted simply in Fig. 9.

The C++ is rather straight forward in progression and function usage (using std::vectors for storage), but it is important to note the flow of coordinates used and how the position- and wave-vectors $\vec{r}$ and $\vec{k}$ are updated. Mostly everything is calculated in Cartesian coordinates with the exception of the parameter grids $n_e(r)$, $B(r)$ and $T_e(r)$. This flow is depicted in Fig. 10. Here the arrows indicate the next step taken in the code, starting from the input position- and wave-vectors, then following the numbering steps in order, such that the necessary gradients are calculated for the ray equations by retrieving the corresponding values in the parameter grids by first converting the position to cylindrical coordinates, then sending the values back to the ray equations. Lastly the vectors are updated by multiplying the resulting dispersion relation gradients by the ray length normalized time steps ds.
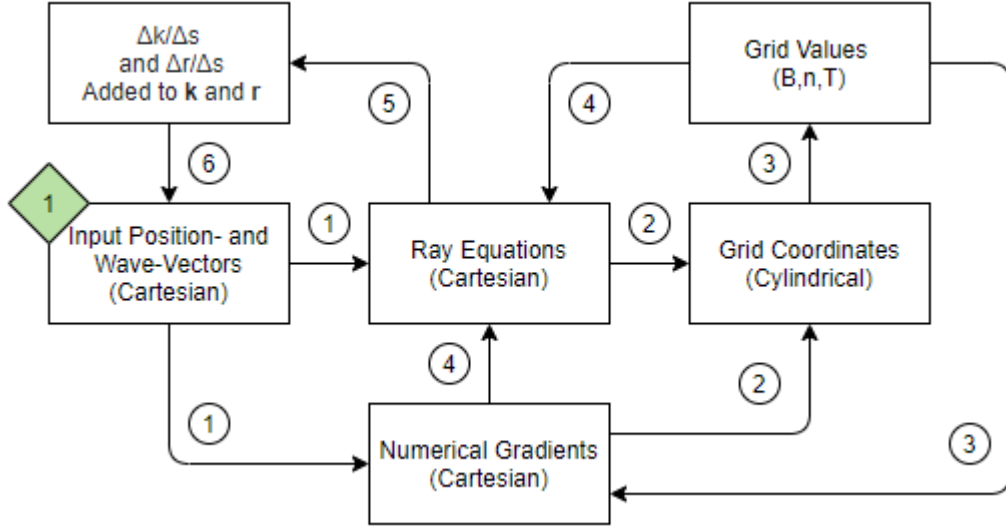
Figure 10: Flowchart illustrating the C++ script layout and how the position- and wave-vectors are updated. In order to determine the parameters in the ray equations, the values of n_e, B and T are stored in grids of cylindrical coordinates R and Z. Starting from the green 1, the general flow of code is depicted using numbered arrows, where the number determines roughly when a function is called or a procedure is done in the ray tracing update loop.

3.4 Simulation Setup

Simulations are done using the Appleton-Hartree and kinetic dispersion relations shown earlier. The situations are designed to be as accurate as possible compared to an experimental setup with a real tokamak using the approximations mentioned in the beginning of this section. The wave modes are tested separately in this section through the ray tracer made for this project. The most probable injection position for diagnostics and heating schemes are from outside the tokamak at $R > 5\,\mathrm{m}$ and $Z = 0\,\mathrm{m}$, since the center area is only $A = 2\pi(2\,\mathrm{m})^2 \approx 25\,\mathrm{m}^2$ for $R < 2\,\mathrm{m}$, which is a very small space for both the electric coil system necessary for upholding the right magnetic fields and any wave-beam-injection diagnostics/heating equipment. The $R_{Stix} = 0$ will correspond to the X-mode cutoff earlier named $R = 0$ in order to distinguish between the cutoff and the radius R. The appropriate ray length step sizes ds and iterations N are found experimentally. The simulations will run from the injection of a wave until the wave collides with the tokamak boundary. For every simulation, first the polaroidal angles ϕ and toroidal angles θ are chosen, then the initial values for the wavenumber k are found theoretically as $k = \sqrt{k_x^2 + k_y^2 + k_z^2}$ through the dispersion relations (2.44) and (2.51), where the coordinates of the wave vector k_x, k_y and k_z are defined using the angles θ to the magnetic field (the magnetic field is defined to be in the toroidal direction). Simulations are done to verify the accuracy of the ray tracer to trace waves of O-, X-mode and Bernstein modes as well as visualize the results of a beam injection through non-monotonic electron densities and the trapping of EBWs in islands.

3.5 Verification by Sub-Results

Writing scripts entails calculation errors and human mistakes. To catch errors and verify the accuracy of the ray tracer, the length of the wave vector k from the ray equations is compared to the theoretical wave number calculated through the corresponding dispersion relation at the current point in space throughout the process. For every simulation, the CMA-diagram is also plotted to ensure the wave

of a certain mode is contained in the physically allowed propagation regimes. Testing is also done by crafting the grid parameter values using constant or linear functions so unexpected behavior is caught early before moving over to the more complex simulations such as Gaussian and potential distributions.
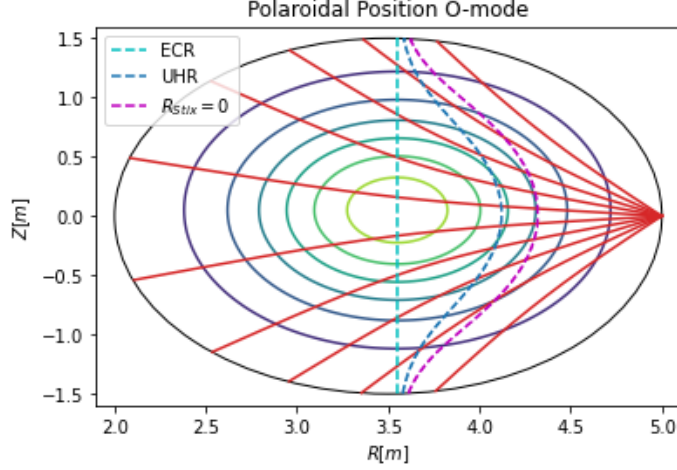
Figure 11: The polaroidal position of O-mode waves (red lines) starting from the outside of the tokamak at $Z = 0$ with angles ϕ varying from $3\pi/4$ to $5\pi/4$ (all with $\theta = \pi/2$ to the magnetic field). The O-mode waves can propagate all throughout the tokamak and are not stopped by the UHR (blue dotted line) or the $R_{Stix} = 0$ cutoff (magenta dotted line). The ECR (cyan dotted line) goes through the center at $R \approx 3.5$.

3.6 Results

3.6.1 O-mode Waves with Appleton-Hartree Dispersion Relation

Rays are cast into the tokamak with parameters as described in section 3.1 using the Appleton-Hartree dispersion relation (2.44) and the ray equations (2.64) and (2.63) using ray-length step sizes of $ds = 0.01$. The resulting polaroidal view (the position in the cross-section of the tokamak ring) are displayed in 11. The ray-length step sizes are chosen by simulating the waves with lower and lower step sizes until the theoretical and simulated wavenumbers are the same. This process is shown in Fig. 12, 13 and 14, where the results of simulating O-mode waves through the designed plasma plotted as the theoretical and simulated wavenumbers k vs the radius with ray-length step sizes $ds = 0.5$, $ds = 0.1$ and $ds = 0.01$ respectively are portrayed. Iterations N are chosen so the waves reach the boundary of the tokamak for every simulated wave in every run. N must be greater for smaller step sizes, yielding $N_{ds=0.5} \approx 10$, $N_{ds=0.1} \approx 50$ and $N_{ds=0.01} \approx 500$. The needed iterations is found by experimentation, since it is indirectly based on the step size ds through the motion of the wave and will be different depending on how the wave propagates through the plasma (note: different angles and different modes yield different necessary iterations). The theoretical values for k should overlap with the simulated values if the ray tracer works, which is clearly not the case for $ds = 0.5$ as seen in Fig. 12. For $ds = 0.1$ in Fig. 13 it is less clear, although they still do not overlap perfectly, so smaller steps must be used. For $ds = 0.01$ in Fig. 14 the theoretical and simulated wavenumbers k are visibly the same, which is why $ds = 0.01$ was chosen for the O-mode wave simulation. In Fig. 15 the O-mode wave propagation can be seen in a CMA-like plot. Since the grids include no limits for the O-mode waves, the waves are free to cross any line except the red $P = 0$ cutoff, which it does not come near.

3.6.2 X-mode Waves with Appleton-Hartree Dispersion Relation

Now using the Appleton-Hartree dispersion relation to calculate the trajectory of an X-mode wave first using step sizes of $ds = 0.002$ as seen in Fig. 17, resulting in unintended behavior. Some of the waves are cut short, and as seen in the CMA-plot of the wave in Fig. 17, the waves jump to
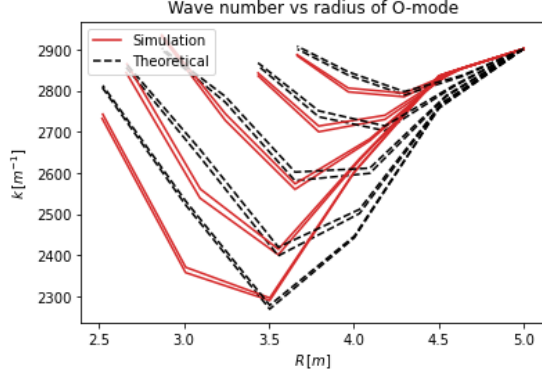
Figure 12: O-mode: the theoretical wavenumber $k = \sqrt{k_x^2 + k_y^2 + k_z^2}$ (black dotted line) found by the Appleton-Hartree dispersion relation (2.44) and the current k used in simulation (red line) calculated from the ray equations (2.64) and (2.63) based on the dispersion relation plotted vs radius with ray length steps of $ds = 0.5$.
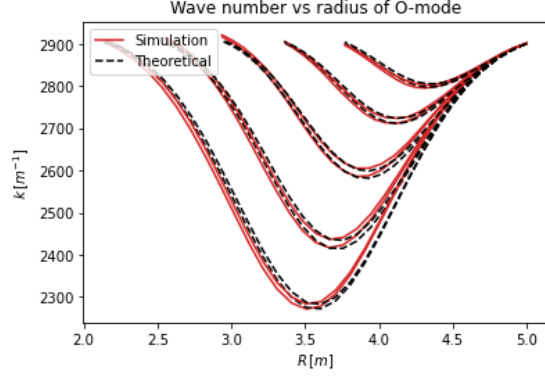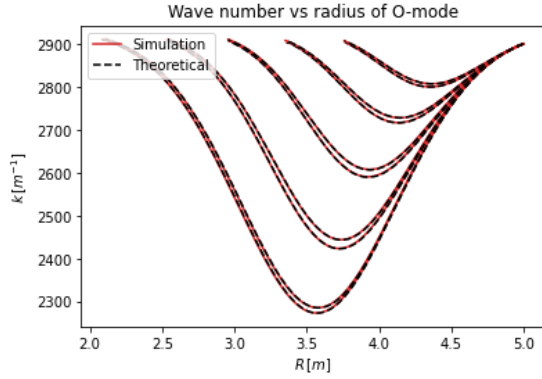

Figure 13: O-mode: the theoretical wavenumber $k = \sqrt{k_x^2 + k_y^2 + k_z^2}$ (black dotted line) found by the Appleton-Hartree dispersion relation (2.44) and the current k used in simulation (red line) calculated from the ray equations (2.64) and (2.63) based on the dispersion relation plotted vs radius with ray length steps of $ds = 0.1$.

Figure 14: O-mode: the theoretical wavenumber $k = \sqrt{k_x^2 + k_y^2 + k_z^2}$ (black dotted line) found by the Appleton-Hartree dispersion relation (2.44) and the current k used in simulation (red line) calculated from the ray equations (2.64) and (2.63) based on the dispersion relation plotted vs radius with ray length steps of $ds = 0.01$.
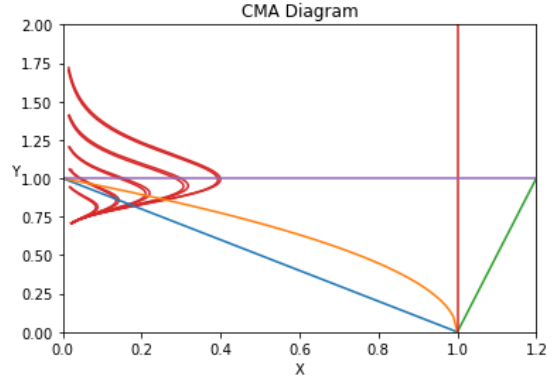
Figure 15: CMA-like figure depicting the O-mode waves (red curved lines) propagating through a plasma. Blue is the $R_{Stix} = 0$ cut-off, orange the UHR, purple the ECR, red the $P = 0$ cutoff and green the $L = 0$ cutoff. The axes are normalized to by the wave frequency ω, $X = \omega_p^2/\omega^2$ and $Y = \omega_c/\omega$.

23
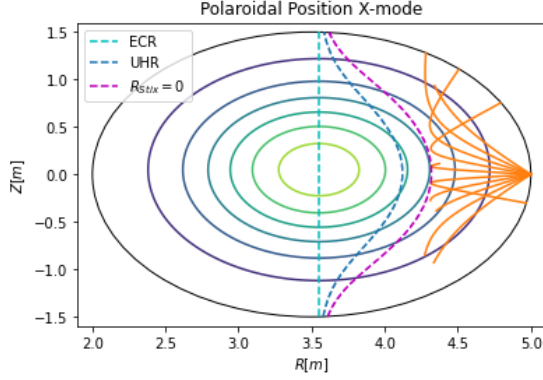
Figure 16: The polaroidal position of X-mode waves (orange lines) starting from the outside of the tokamak at $Z = 0$ with angles ϕ varying from $\phi = 3\pi/4$ to $\phi = 5\pi/4$ (all with $\theta = \pi/2$ to the magnetic field) using the Appleton-Hartree dispersion relation. Unintended behavior occurs at low step sizes of $ds = 0.002$. The X-mode waves cannot propagate through the UHR (blue dotted line) or $R_{Stix} = 0$ cutoff (magenta dotted line) as seen in the figure. The ECR (cyan dotted line) goes through the center at $R \approx 3.5$.
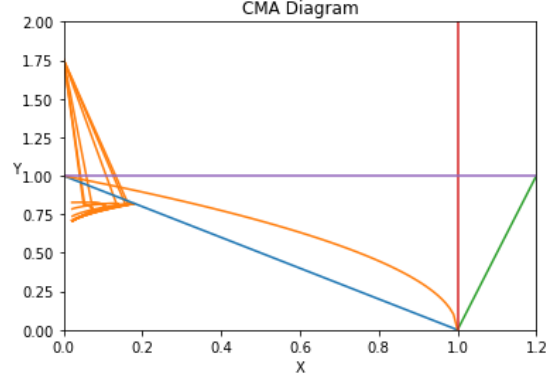
Figure 17: CMA-like figure depicting the X-mode waves (orange curved lines) propagating through a plasma using the Appleton-Hartree dispersion relation. Blue is the $R_{Stix} = 0$ cutoff, orange the UHR, purple the ECR, red the $P = 0$ cutoff and green the $L = 0$ cutoff. The axes are normalized to by the wave frequency ω, $X = \omega_p^2/\omega^2$ and $Y = \omega_c/\omega$. The X-mode waves cannot propagate through the $R_{Stix} = 0$ cutoff.

$Y \approx 1.75$. Noting that this is the same end spot for the furthest reaching O-mode waves (closest to the center of the tokamak for largest magnetic field strength), the simulations are again done for larger step sizes. In Fig. 18 the simulated trajectory of X-mode waves using the Appleton-Hartree dispersion relation are shown for $ds = 0.01$. The corresponding CMA-plot found in Fig. 19 also shows the waves approaching the $R_{Stix} = 0$ cutoff and then being reflected.

3.6.3 O- and X-mode Injection into Overdense Plasma

Results of simulating injection of O- and X-mode waves into an overdense plasma are shown in Fig. ?? for the trajectory and in Fig. 21. Here it is visible that the O-mode waves cannot propagate beyond the $P = 0$ cutoff at $X = \frac{\omega_{pe}^2}{\omega^2} = 1$. X-mode waves are still halted by the $R_{Stix} = 0$ cutoff, but the O-mode can no longer enter the center, which normally is necessary for heating schemes as the goal is to hit the ECR.

3.6.4 X-mode and Electron Bernstein Waves with Kinetic Dispersion Relation

Using the same procedure as for the O-mode waves, the X-mode waves using the kinetic dispersion relation (2.51) are tested using the ray equations 2.64 and 2.63. Starting by testing the simulated against theoretical wavenumbers as seen in Fig. 22 and 23 it is evident that step sizes of $ds = 0.01$ in Fig. 22 are too large and do not produce accurate results. Taking it up a notch the step sizes are reduced to $ds = 0.0002$ in Fig. 23. In Fig. 24 the polaroidal view of the kinetic X-mode wave propagation is plotted, where it is visible that the X-mode waves cannot propagate through the $R_{Stix} = 0$ cutoff or the upper hybrid resonance as expected. This is also visible in the CMA-plot in Fig. 25.

Using the kinetic dispersion relation to simulate X-mode waves injected from the center of the tokamak at $R = 2$m, the results are shown in Fig. 26. Here the ray trajectory goes through the
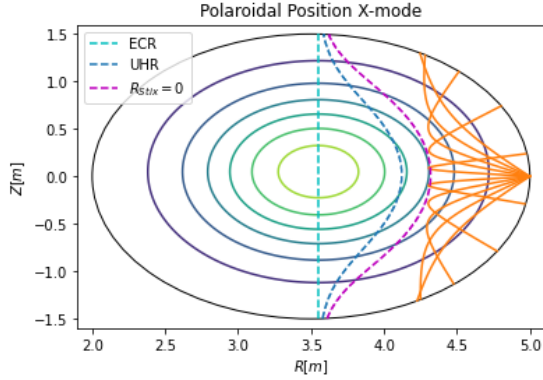
Figure 18: The polaroidal position of X-mode waves using the Appleton-Hartree dispersion relation (orange lines) starting from the outside of the tokamak at $Z = 0$ with angles ϕ varying from $\phi = 3\pi/4$ to $\phi = 5\pi/4$ (all with $\theta = \pi/2$ to the magnetic field). The X-mode waves cannot propagate through the UHR (blue dotted line) or $R_{Stix} = 0$ cutoff (magenta dotted line) as seen in the figure. The ECR (cyan dotted line) goes through the center at $R \approx 3.5$.
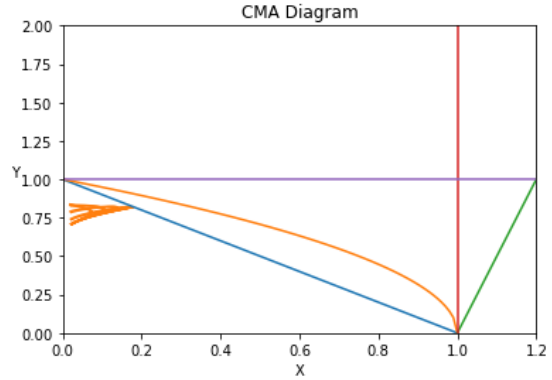
Figure 19: CMA-like figure depicting the X-mode waves (orange curved lines) propagating through a plasma using the Appleton-Hartree dispersion relation with $ds = 0.01$. Blue is the $R_{Stix} = 0$ cutoff, orange the UHR, purple the ECR, red the $P = 0$ cutoff and green the $L = 0$ cutoff. The axes are normalized to by the wave frequency ω, $X = \omega_p^2/\omega^2$ and $Y = \omega_c/\omega$. The X-mode waves cannot propagate through the $R_{Stix} = 0$ cutoff.

plasma and reaches the upper hybrid resonance, then is sent back out towards the center of the tokamak in a more curved fashion than they had going in. Looking at the CMA-plot in Fig. 27 the waves return using a different path with generally a higher electron density than they came in. This is the result of a slow X-mode electron Bernstein conversion at the UHR, as is seen in Fig. 28. Here the simulated wavenumbers at different radii (orange) correspond to the theoretical X-mode wavenumbers coming in, but as the waves return, they correspond to the theoretical EBW wavenumbers, thus a conversion from slow X-mode to EBW is made at the UHR.

3.6.5 Introducing Islands to O- and X-mode Waves

Now simulations are done after introducing an island to simulate disturbances in the plasma. The island corresponds to a spike in electron density and electron temperature at $R \approx 4.5\,\mathrm{m}$ with a slightly greater peak than the original Gaussian peak. The newly introduced island spike is also a Gaussian distribution. Results obtained when injecting O- and X-mode waves from the outside of the tokamak at $R = 5\,\mathrm{m}$ and $Z = 0\,\mathrm{m}$ are shown in Fig. 29 using step sizes $ds = 0.0002$. Here the upper hybrid resonance and the $R_{Stix} = 0$ cutoff are shifted and curl around the island. As a result, the O-mode waves are bent earlier due to the island, and the X-mode waves are rejected earlier due to the new location of the $R_{Stix} = 0$ cutoff. The CMA-plot in Fig. 30 shows normalized frequencies corresponding to the beam trajectories. A wavenumber test shown in Fig. 31 shows the simulated wavenumbers following the theoretical wavenumbers at different radii. In Fig. 32 the theoretical wavenumber k for X-mode and EBWs at radii around the island is shown. Here it is visible that EBWs cannot propagate further away than $R \approx 4.6\,\mathrm{m}$ corresponding to the UHR. At larger radii the density becomes too small for EBWs to propagate, although the X-mode can again propagate at $R \approx 4.8\,\mathrm{m}$ corresponding to the $R_{Stix} = 0$ cutoff.
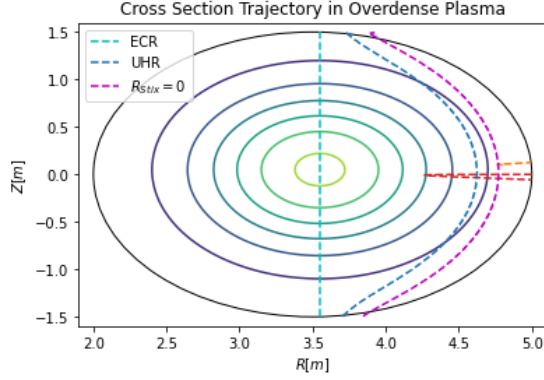
Figure 20: Beam trajectory of an O- and an X-mode wave injected into an overdense plasma with peak electron density $n_e = 5\,10^{20}\,\mathrm{m}^{-3}$. The X-mode wave (orange dotted line) is rejected at the $R_{Stix} = 0$ cutoff, while the O-mode (red dotted line) is rejected at $X = 1$.
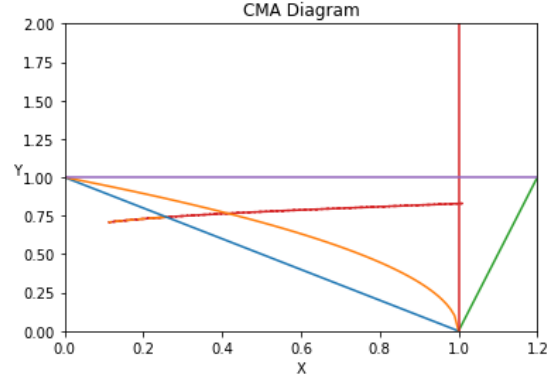
Figure 21: CMA-like plot of the O- and X-mode waves injected into an overdense plasma with peak electron density $n_e = 5\,10^{20}\,\mathrm{m}^{-3}$. The X-mode wave (orange dotted line) is rejected at the $R_{Stix} = 0$ cutoff, while the O-mode (red dotted line) is rejected at $X = 1$.

3.6.6 Trapped EBW in Island

After introducing the island to O- and X-mode a simulation of the EBWs is done. Electron Bernstein waves are introduced in the plasma starting at $R = 4.4\,\mathrm{m}$ and $Z = 0\,\mathrm{m}$ with angles of $\phi_1 = \pi/2$ and $\phi_2 = 5/4\,\pi$. The results are shown in Fig. 33. The zoomed in figure shows the trajectories encountering the UHR multiple times before escaping through the opening located at $R \approx 4.15\,\mathrm{m}$ and $Z \approx [-0.2, 0.2]\,\mathrm{m}$. In Fig. 35 a corresponding CMA-plot is shown. A wavenumber test is shown in Fig. 34, where it is visible the waves follow the theoretical EBW wavenumbers throughout the simulation.
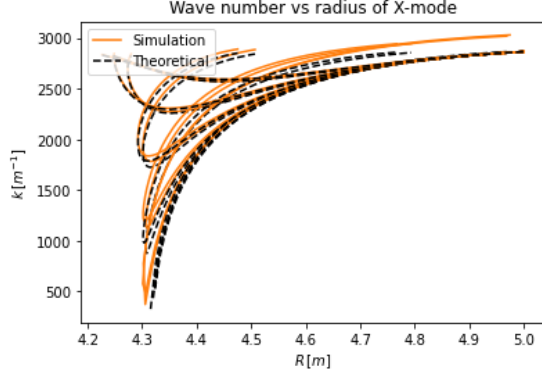
Figure 22: X-mode: the theoretical wavenumber $k = \sqrt{k_x^2 + k_y^2 + k_z^2}$ (black dotted line) found by the kinetic dispersion relation (2.51) and the current k used in simulation (orange line) calculated from the ray equations (2.64) and (2.63) based on the dispersion relation plotted vs radius with ray length steps of $ds = 0.01$.
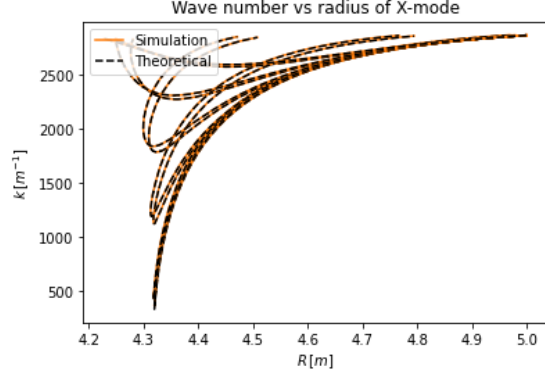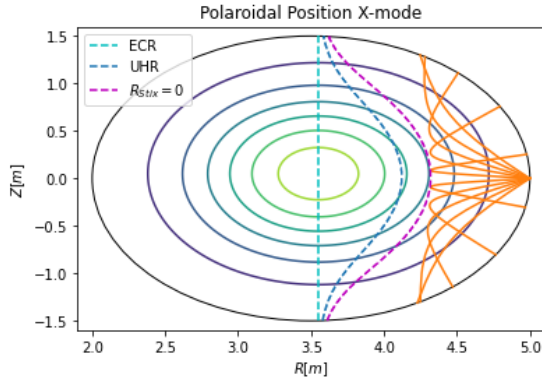
Figure 23: X-mode: the theoretical wavenumber $k = \sqrt{k_x^2 + k_y^2 + k_z^2}$ (black dotted line) found by the kinetic dispersion relation (2.51) and the current k used in simulation (orange line) calculated from the ray equations (2.64) and (2.63) based on the dispersion relation plotted vs radius with ray length steps of $ds = 0.0002$.

Figure 24: The polaroidal position of X-mode waves (orange lines) starting from the outside of the tokamak at $Z = 0$ with angles ϕ varying from $\phi = 3\pi/4$ to $\phi = 5\pi/4$ (all with $\theta = \pi/2$ to the magnetic field). The X-mode waves cannot propagate through the UHR (blue dotted line) or $R_{Stix} = 0$ cutoff (magenta dotted line) as seen in the figure. The ECR (cyan dotted line) goes through the center at $R \approx 3.5$.
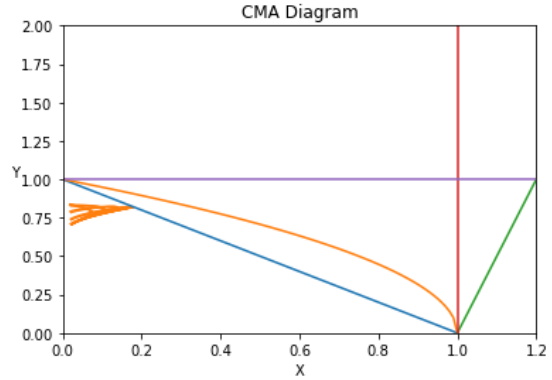
Figure 25: CMA-like figure depicting the X-mode waves (orange curved lines) propagating through a plasma. Blue is the $R_{Stix} = 0$ cutoff, orange the UHR, purple the ECR, red the $P = 0$ cutoff and green the $L = 0$ cutoff. The axes are normalized to by the wave frequency ω, $X = \omega_p^2/\omega^2$ and $Y = \omega_c/\omega$. The X-mode waves cannot propagate through the $R_{Stix} = 0$ cutoff.
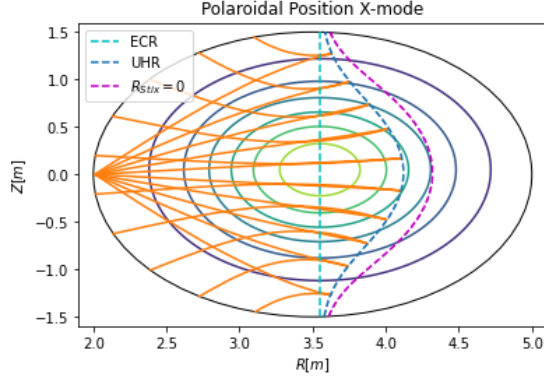
Figure 26: The polaroidal position of kinetic X-mode waves (orange lines) starting from the outside of the tokamak at $Z = 0$ with angles ϕ varying from $3\pi/4$ to $5\pi/4$ (all with $\theta = \pi/2$ to the magnetic field). The X-mode waves cannot propagate through the UHR (blue dotted line) or $R_{Stix} = 0$ cutoff (magenta dotted line), and are here interrupted by the $R_{Stix} = 0$ cutoff. The ECR (cyan dotted line) goes through the center at $R \approx 3.5$.
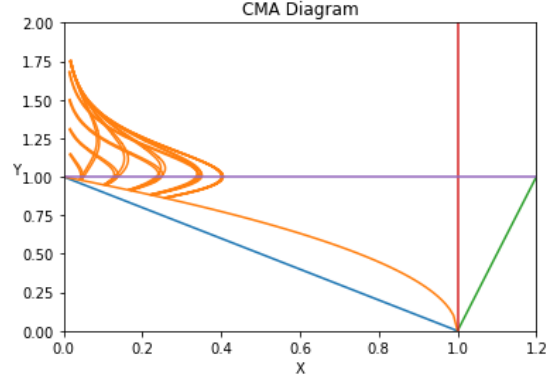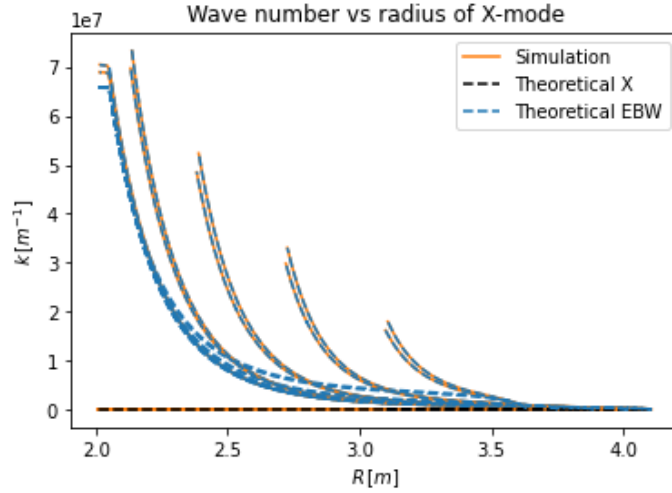
Figure 27: CMA-like figure depicting the X-mode waves (orange curved lines) propagating through a plasma when injected from the center of the tokamak. Blue is the $R_{Stix} = 0$ cutoff, orange the UHR, purple the ECR, red the $P = 0$ cutoff and green the $L = 0$ cutoff. The axes are normalized to by the wave frequency ω, $X = \omega_p^2/\omega^2$ and $Y = \omega_c/\omega$.

Figure 28: X-mode: the theoretical wavenumber $k = \sqrt{k_x^2 + k_y^2 + k_z^2}$ (black dotted line for the X-mode and blue dotted line for EBW) found by the kinetic dispersion relation (2.51) and the current k used in simulation (orange line) calculated from the ray equations (2.64) and (2.63) based on the dispersion relation plotted vs radius with ray length steps of $ds = 0.0002$. The simulation corresponds to waves first following theoretical EBW then the theoretical X-mode, thus showing a conversion from X-mode waves to Bernstein waves.
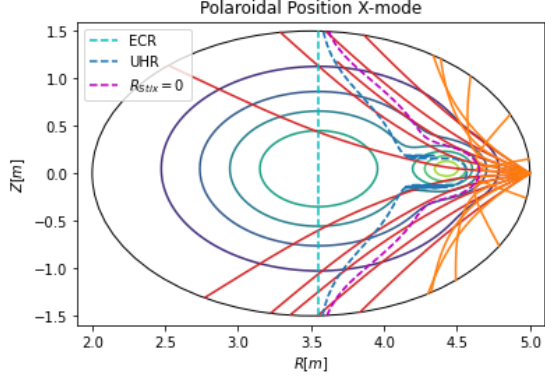
Figure 29: The polaroidal position of O- and X-mode waves (red and orange lines) starting from the outside of the tokamak at $Z = 0$ with angles ϕ varying from $\phi = 3\pi/4$ to $\phi = 5\pi/4$ (all with $\theta = \pi/2$ to the magnetic field). The X-mode waves cannot propagate through the UHR (blue dotted line) or $R_{Stix} = 0$ cutoff (magenta dotted line) as seen in the figure. The ECR (cyan dotted line) goes through the center at $R \approx 3.5$.
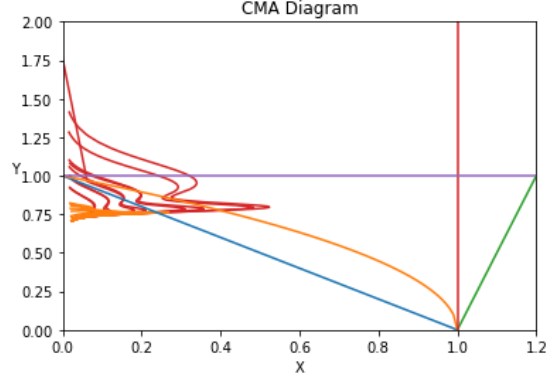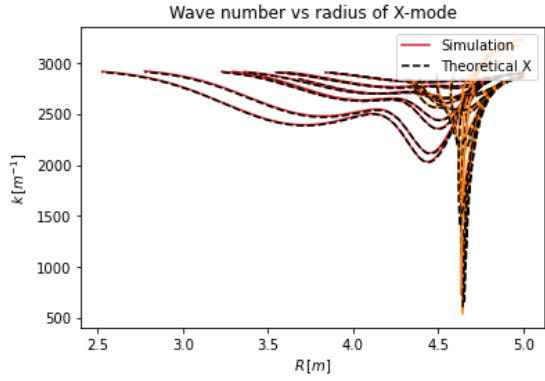

Figure 30: CMA-like figure depicting the O- and X-mode waves (red and orange curved lines) propagating through a plasma. Blue is the $R_{Stix} = 0$ cutoff, orange the UHR, purple the ECR, red the $P = 0$ cutoff and green the $L = 0$ cutoff. The axes are normalized to by the wave frequency ω, $X = \omega_p^2/\omega^2$ and $Y = \omega_c/\omega$. The X-mode waves cannot propagate through the $R_{Stix} = 0$ cutoff.

Figure 31: O- and X-mode: the theoretical wavenumber $k = \sqrt{k_x^2 + k_y^2 + k_z^2}$ (black dotted line) and the simulated k used in simulation (red and orange line) vs radius with ray length steps of $ds = 0.0002$.
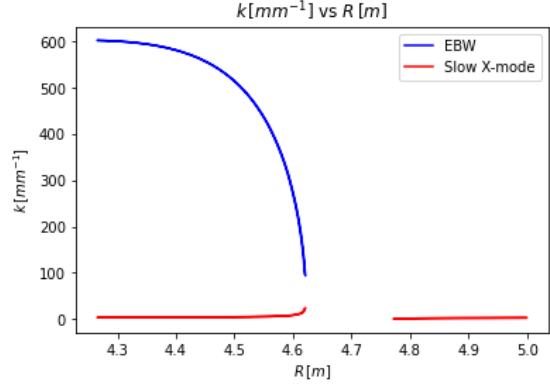

Figure 32: Plot of the theoretical wavenumbers k for X-mode and EBWs around the location of the island. A range between $R4.6\,\text{m}$ and $R4.8\,\text{m}$ have no corresponding wavenumber as these radii correspond to the local UHR and $R_{Stix} = 0$ cutoff. EBWs can only propagate in relatively high density, thus it only exists to the left of the UHR.
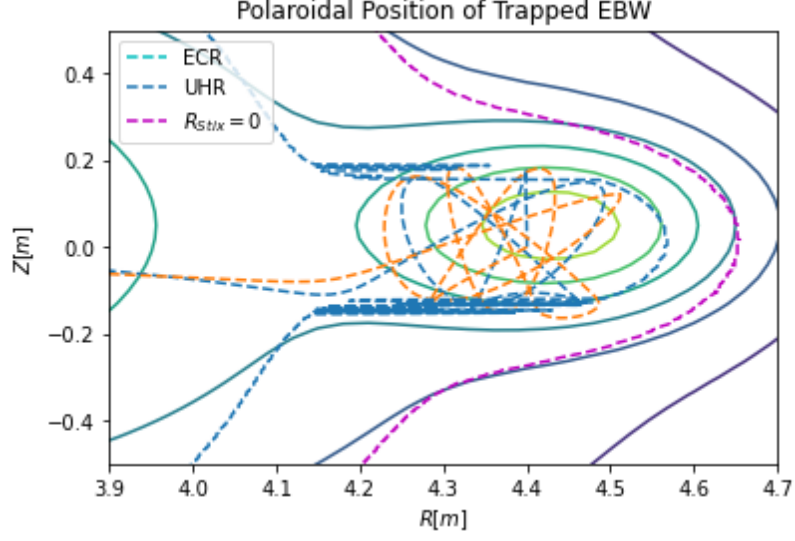
Figure 33: The polaroidal position of two trapped electron Bernstein waves (orange and blue dotted lines) starting from $R = 4.4$ and $Z = 0$ with angles $\phi_1 = \pi/2$ and $\phi_2 = \pi5/4$(all with $\theta = \pi/2$ to the magnetic field). The EBWs cannot propagate through the UHR (blue dotted line) or $R_{Stix} = 0$ cutoff (magenta dotted line), and are here interrupted by the $R_{Stix} = 0$ cutoff multiple times, thus are considered trapped. The ECR (cyan dotted line) goes through the center at $R \approx 3.5$.
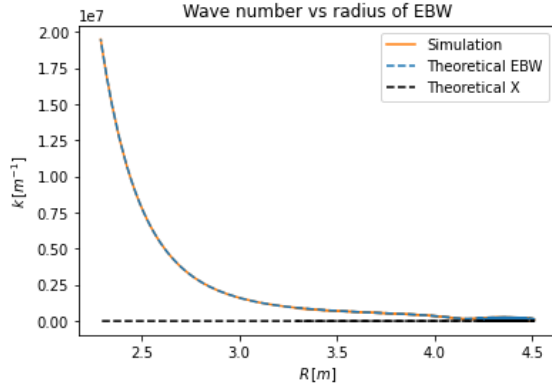
Figure 34: EBW: the theoretical wavenumber $k = \sqrt{k_x^2 + k_y^2 + k_z^2}$ (black dotted line for the X-mode and blue dotted line for EBW) found by the kinetic dispersion relation (2.51) and the current k used in simulation (orange line) calculated from the ray equations (2.64) and (2.63) based on the dispersion relation plotted vs radius with ray length steps of $ds = 0.00001$. The simulation follows the theoretical electron Bernstein wavenumbers.
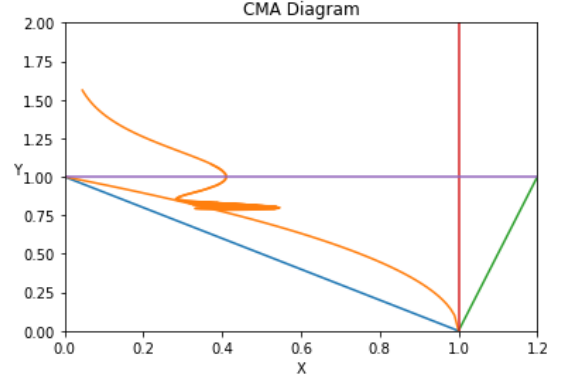

Figure 35: CMA-like figure depicting the electron Bernstein waves (orange curved lines) trapped in an electron density island. Blue is the $R_{Stix} = 0$ cutoff, orange the UHR, purple the ECR, red the $P = 0$ cutoff and green the $L = 0$ cutoff. The axes are normalized to by the wave frequency ω, $X = \omega_p^2/\omega^2$ and $Y = \omega_c/\omega$.

4 Discussion

The simulations are based on an artificial tokamak mimicking the geometry and parameters used in real tokamaks. From the results of simulations using the ray tracer, the ray tracer works as intended given the right step sizes for numerical approximation. Using the Appleton-Hartree dispersion relation for cold plasma (2.44), the ordinary wave mode is simple to describe mathematically, and by convergence tests is also the one requiring the least calculations to be accurate as seen in the results. Good results are observed using the ray tracer for step sizes of $ds = 0.01$. Results of simulation of the extraordinary wave trajectories using the kinetic dispersion relation (2.51) shows accuracy at $ds = 0.0002$, which can still be considered fast. When using the ray tracer based on the Appleton-Hartree dispersion relation for X-modes however, issues occurred when using step sizes of $ds = 0.0002$, where the ray would "leap" to the edge radius limit at $R = 2\,\mathrm{m}$. Dialing back to $ds = 0.01$ results in less accurate results as seen in Fig. 22 and Fig. 23, where the simulated wavenumbers better matches the theoretical wavenumbers for $ds = 0.002$, but the overall trajectory still follows the expected trajectory as seen in Fig. 18, which compared to the slow X-mode ray tracing using the kinetic dispersion relation in Fig. 24 seems to yield the same results. For the kinetic dispersion relation by injecting beams from the center of the artificial tokamak where the magnetic field is greatest, the beams reach the upper hybrid resonance, where the slow X-mode beams are converted to electron Bernstein waves as proposed by [7] and seen in Fig. 26 for the trajectory and 28 for the wavenumber behaviors, where the simulation visibly follows the theoretical EBW wavenumbers. A step size of $ds = 0.00001$ is needed to properly simulate the EBWs, which results in very large simulation times. This is likely due to the large wavenumbers as opposed to O- and X-mode, although the ray equations utilize ray length step instead of time steps.

Results of the ray tracing of O-, X-mode and EBWs when an island is added for an underdense plasma, the O-mode traverses through as expected, although the path is drastically changed depending greatly on the initial poloidal angle. In 33 simulations are done of EBWs starting at radius $R = 4.4\,\mathrm{m}$ with different angles. Whenever the waves intercept the UHR, they are reflected, thus effectively being trapped, and finally after many iterations, they escape. Noting that this is an ideal system, where the totality of the waves are reflected when met with a cutoff, in reality some of the energy should dissipate in a wave transmitted through the barrier.

Geometrical optics assumes very small changes in a length scale compared to the wavelength of the injected waves, which may not be the case for plasmas. Since the results of simulations behave mostly as expected, the ray tracer appears to work for the linear waves, but when visiting non-linear physical effects, one must be wary.

5   Conclusion and Further Work

In this thesis waves propagating through plasmas have been studied, specifically the ordinary and extraordinary wave modes found from a zero temperature approximation of the plasma and the slow extraordinary and electron Bernstein waves found by a kinetic approach, first by theoretically describing the waves based on relevant assumptions and derivation, then by writing a ray tracer to trace the linear waves through plasma of varying density structures. Wave propagation through a plasma have been described by dispersion relations, where the possible modes are found by considering a plasma a dielectric medium. The ray tracer has been presented and verified through results of simulation, where the trajectory of ordinary, extraordinary and electron Bernstein Waves through an artificial tokamak plasma are calculated and evaluated. Rays of varying poloidal angle have been simulated as the wave modes worked with in this thesis propagate perpendicularly to the magnetic field, and the magnetic field has been made to follow the toroidal direction. The simulated wavenumbers have also been plotted, where the initial condition of the wavevector is based on the calculated theoretical wavenumber in the injection position from barely inside the outer walls of the tokamak and the initial angles. The ray tracer appears to work for both the Appleton-Hartree and the kinetic dispersion relation, although through convergence checks the numerical step sizes must be in an appropriate range; EBWs require the smallest numerical steps, X-mode the second smallest and O-mode the least small steps to be accurate. Multiple simulations have been done to verify the simulated behavior is as expected.

Processes such as the decay of waves and three wave interactions leads to the possibility of "new" waves forming in regions of the tokamak other than the injection area. Simulations using the ray tracer by injecting X-mode and EBWs straight into the middle of a plasma island in the tokamak cross section have been made to show the possible entrapment of waves due to the resulting shape of the upper hybrid resonance propagation boundary. Thus a possible consequence of time-dependent deformities of the density structure in a plasma has been shown, which in turn can lead to destructive behavior. The ray tracer may be used for other specific cases, such as heating schemes and diagnostics. By varying the density structure the propagation boundaries can be varied as well resulting in specific behavior from each of the wave modes, O, X and EBWs. Further investigations of for example parametric decay instabilities can be made using the using the ray tracer as simulation tool, where more wave propagations in structures such as islands can be made to assist the theoretical results. The ray tracer could also be expanded to be able to describe more than O-mode, X-mode and EBWs, as example the edge localized modes occuring in the edge regions of a tokamak plasma.

6   References

[1] Arfken, George B. & Weber, Hans J. *Mathematical Methods for Physicists; 6th. ed.* Elsevier Academic Press, Miami University   University of Virginia, 2005.

[2] Bartels, Sören. *Numerical Approximation of Partial Differential Equations.* Springer International Publishing, Angewandte Mathematik, 2016.

[3] Bellan, Paul M. *Fundamentals of Plasma Physics.* Cambridge University Press, California Institute of Technology, 2006.

[4] Chen, Francis F. *Introduction to Plasma Physics and Controlled Fusion.* Springer, University of California, Los Angeles, 2016.

[5] Freidberg, Jeffrey P. *Plasma physics and fusion energy.* Cambridge University Press, Engineering Department, 2007.

[6] Griffiths, David J. *Introduction to electrodynamics; 4th. ed.* Pearson, Boston, MA, 2013. Republished by Cambridge University Press in 2017.

[7] Hansen, S. K. *Parametric Decay Instabilities in the Electron Cyclotron Resonance Heating Beams at ASDEX Upgrade*, 2019. Technical University of Denmark, Department of Physics and Max-Planck-Institut für Plasmaphysik.

[8] Hartfuß, Hans Jurgen & Geist, Thomas. *Fusion Plasma Diagnostics With Mm-waves: an Introduction.* Wiley-VCH Verlag, Max-Planck-Institut fur Plasmaphysik (IPP), 2013.

[9] Harvey, James E.; Irvin, Ryan G. & Pfisterer, Richard N. Modeling physical optics phenomena by complex ray tracing. *Optical Engineering — 2015, Volume 54, Issue 3, pp. 141706*, 2015.

[10] Haupt, Kirsten.   Fusion Machines: Searching for the Perfect Shape.   `https://www.iter.org/newsline/-/3037`.   Online; Last Visit: 18/12 - 2021. Original source of image: EUROfusion/EFDA-JET.

[11] Hecht, E. *Optics; 5th ed.* Pearson, 2017.

[12] Mazzucato, Ernesto. *Electromagnetic Waves for Thermonuclear Fusion Research.* World Scientific Publishing Co., Princeton Plasma Physics Laboratory, 2014.

[13] Mills, D. L. *Nonlinear Optics: Basic Concepts.* Springer Berlin Heidelberg, 1991.

[14] Senstius, M. G. et al. Plasma Phys. Control. Fusion 62 . *025010*, 2020.

[15] Shevchenko, V.1; Cunningham, G.1; Gurchenko, A.; Gusakov, E.; Lloyd, B.; O'Brien, M.; Saveliev, A.; Surkov, A.; Volpe, F.; Walsh, M. Development of electron Bernstein wave research in mast. *Fusion Science and Technology — 2007, Volume 52, Issue 2, pp. 202-15*, 2007.
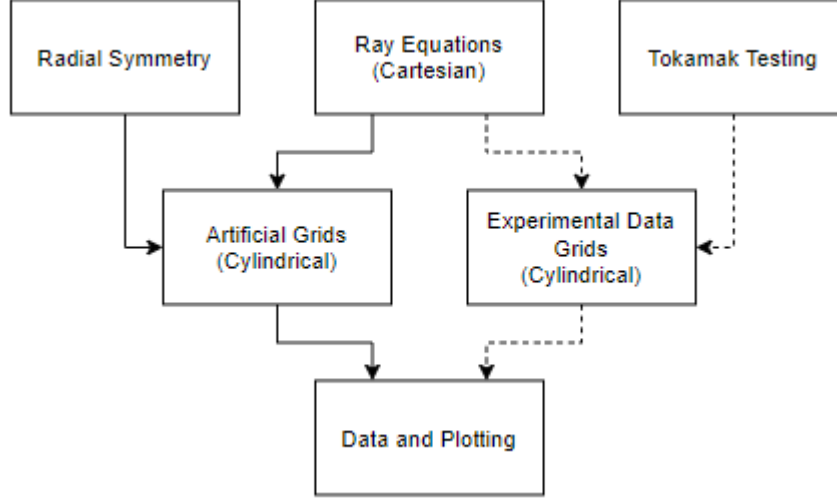
Figure 36: Flowchart illustrating the possibility of swapping the artificial grids from the symmetric analysis with experimentally found grids.

7 Appendix

7.1 EBW

The electric susceptibility $X(\vec{k}, \omega)$ as found in [7]:

$$X(\vec{k}, \omega) = \frac{2\omega_{pe}^2}{v_{Te}^2} \frac{1 + \frac{\omega + i\nu_e}{k_\parallel v_{Te}} \sum_{n=-\infty}^{\infty} I_n(k_\perp^2 r_{Le}^2) e^{-k_\perp^2 r_{Le}^2} \mathcal{Z}\left(\frac{\omega + i\nu_e - n\omega_{ce}}{k_\parallel v_{Te}}\right)}{1 + \frac{i\nu_e}{k_\parallel v_{Te}} \sum_{n=-\infty}^{\infty} I_n(k_\perp^2 r_{Le}^2) e^{-k_\perp^2 r_{Le}^2} \mathcal{Z}\left(\frac{\omega + i\nu_e - n\omega_{ce}}{k_\parallel v_{Te}}\right)}. \tag{7.1}$$

where ν_e is the electron collision frequency, I_n is a modified Bessel function of first kind of order n, $\mathcal{Z}(\zeta) = (1/\sqrt{\pi}) \int_{-\infty}^{\infty} e^{\zeta^2}/(\epsilon - \zeta)\, d\epsilon$ is the Fried-Conte plasma dispersion function.

7.2 Numerical flowchart

In Fig. 36 a flowchart is made to show the possibility of rewriting the ray tracer to be used on experimentally found data instead of the approximated artificial grids.
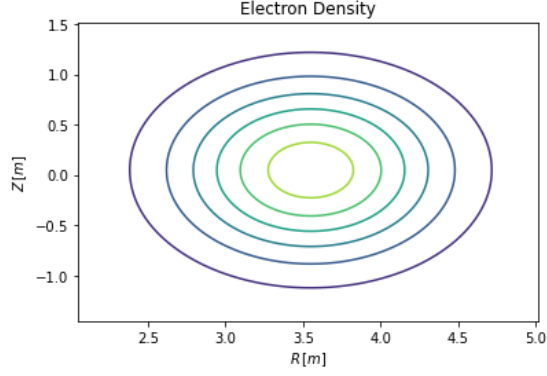
7.3 Density Figures

Figure 37: Contour plot of the electron density distribution as a Gaussian distribution with peak at the middle of the cross-section of the tokamak ring ($R = 3.5$ m, $Z = 0$ m) with Radius vs. Z-axes. Peak electron density is $n_e = 10^{20}$ m^{-3} (see Fig. 38).
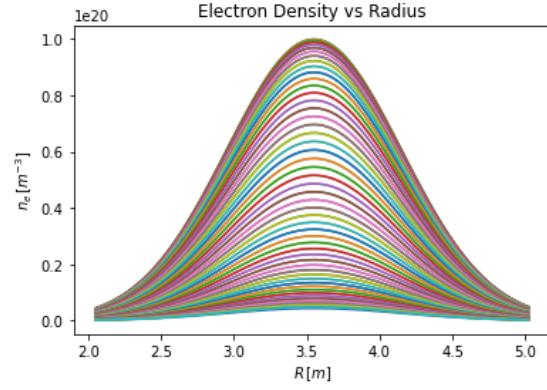

Figure 38: Electron density vs. Radius over many values of Z. The electron density distribution is a Gaussian distribution with peak at ($R = 3.5$ m, $Z = 0$ m). Peak electron density is $n_e = 10^{20}$ m^{-3}.
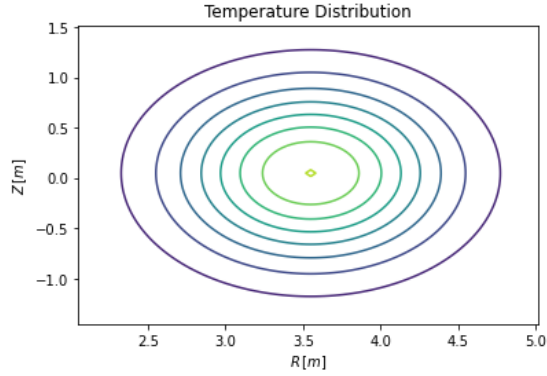

Figure 39: Contour plot of the temperature distribution as a Gaussian distribution with peak at the middle of the cross-section of the tokamak ring ($R = 3.5$ m, $Z = 0$ m) with Radius vs. Z-axes. Peak temperature is $T_e = 10e = 1.6\,10^{-18}$ eV (see Fig. 40).
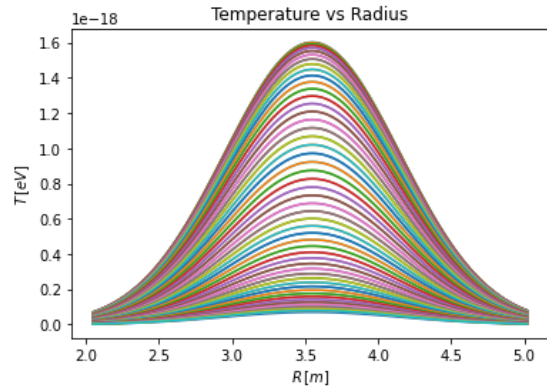

Figure 40: Temperature vs. Radius over many values of Z. The temperature distribution is a Gaussian distribution with peak at ($R = 3.5$ m, $Z = 0$ m). Peak temperature is $T_e = 10e = 1.6\,10^{-18}$ eV.
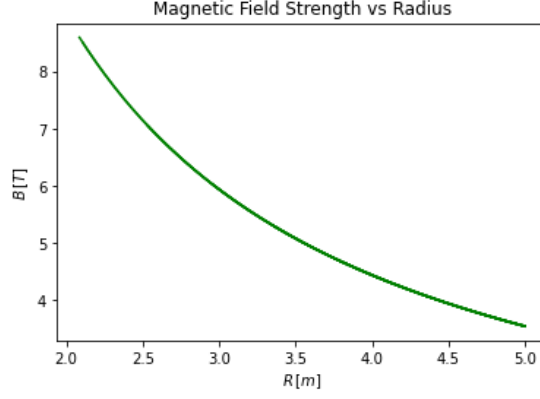
Figure 41: Magnetic field strength as function of the radius R. Measured in Tesla, the magnetic field strength varies as $B \propto 1/R$. The proportionality value for the magnetic field strength is chosen so the ECR is in the center of the cross-section of the tokamak ring, thus at $R = 3.5\,\mathrm{m}$, with a value of $\omega = \omega_c = eB(3.5)/m_e \iff B(3.5) = m_e\omega/e \approx 5\,\mathrm{T}$.
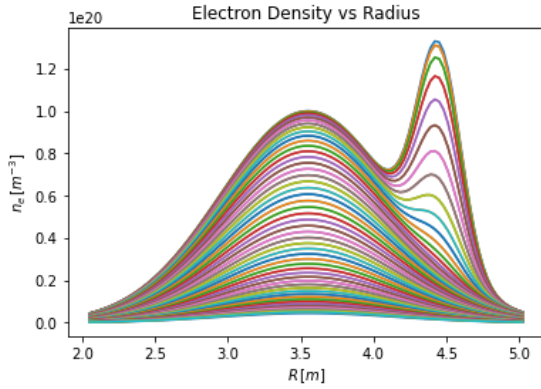

Figure 42: The electron density vs radius when an island is added. The main electron density peak is $n_e = 10^{20}\,\mathrm{m}^{-3}$, while the island peak is slightly greater.
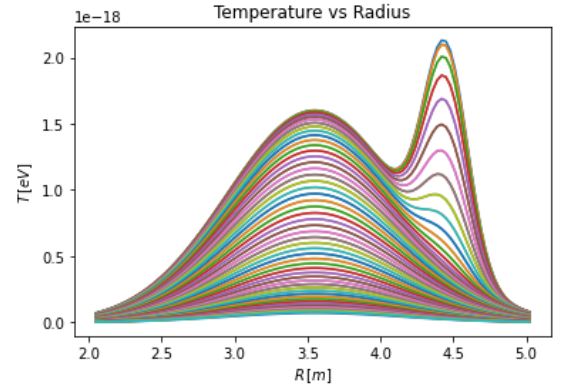

Figure 43: The electron temperature vs radius when an island is added. The main electron temperature peak is $T_e = 10\,\mathrm{e} = 1.6\,10^{-18}\,\mathrm{eV}$, while the island peak is slightly greater.
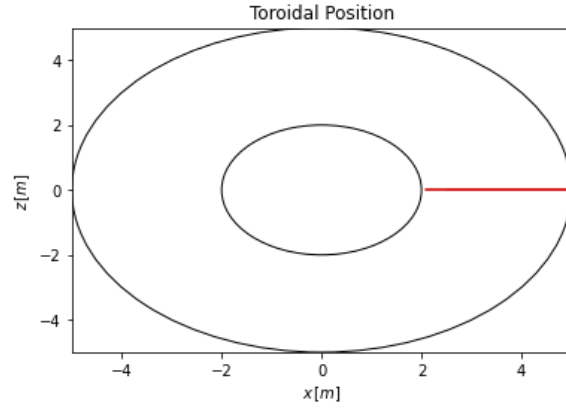
Figure 44: The toroidal position of O-mode waves (red line) starting from the outside of the tokamak at $Z = 0$ with angles ϕ varying from $\phi = 3\pi/4$ to $\phi = 5\pi/4$ (all with $\theta = \pi/2$ to the magnetic field). Since the magnetic field is assumed to follow the torus directly, changes in ϕ play no apparent role when viewing the toroidal position, where only θ is visible.